ACS Catalysis

Open Access
This article is licensed under CC-BY 4.0

pubs.acs.org/acscatalysis
Research Article

# The Synergetic Effect of $Cu^{+}/Cu^{2+}$ in Unsupported $Cu_xO$ on the Activity and Mechanism of Low-Temperature CO Oxidation: A Transient Kinetic and Isotopic Study

Michalis A. Vasiliades,[§] Georgia-Maria D. Zarkou,[§] Cheng Zhang, Alexandra Theodosiou, Mirko Prato, Sašo Gyergyek, Petar Djinović, Sotirios Christodoulou,* and Angelos M. Efstathiou*

Cite This: *ACS Catal.* 2026, 16, 5499−5519
Read Online

ACCESS | Metrics & More | Article Recommendations | Supporting Information

**ABSTRACT:** This work has been motivated by the lack of knowledge concerning the influence of the surface $Cu^{+}/Cu^{2+}$ molar ratio on the composition and reactivity of the adsorbed phase established on the unsupported $Cu_2O$-CuO solids during CO oxidation in excess oxygen (1% CO/20% $O_2$/He) and at low temperatures ($T$ < 200 °C). Variation of the $Cu^{+}/Cu^{2+}$ ratio was achieved under controlled calcination conditions applied on an initially c-$Cu_2O$ synthesized by the colloidal method. The influence of the $Cu^{+}/Cu^{2+}$ molar ratio on the mechanism of CO oxidation (Langmuir−Hinshelwood, Mars−van Krevelen, or Eley−Rideal), the surface concentration of active CO-s and COO-s reaction intermediates, and the thermal stability of carbonate-type adsorbed inactive species formed on the working catalytic surface were derived using the SSITKA technique combined with mass spectrometry and *in situ* DRIFTS. It was found that for high $Cu^{+}/Cu^{2+}$ molar ratio values (ca. ∼4.9), CO oxidation follows an Eley−Rideal mechanism, where gaseous CO reacts mainly with labile lattice oxygen species. Reversibly chemisorbed CO ($\theta \sim 0.15$) was measured, but this was not in the CO oxidation path. On the other hand, for low $Cu^{+}/Cu^{2+}$ molar ratio values (ca. 0.01−0.025), the mechanism shifts toward M-vK type, where the concentration of active COO-s was found to increase with increasing $Cu^{2+}/Cu^{+}$ molar ratio. Two types of linear adsorbed CO-s were identified by SSITKA-DRIFTS under working reaction conditions, and these were associated with $Cu^{2+}$ and $Cu^{+}$ sites. The ratio of the two adsorbed CO species did not vary proportionally with the $Cu^{+}/Cu^{2+}$ ratio. The specific CO oxidation rate (per gram or $m^2$ of $Cu_xO$) was found to increase with increasing $Cu^{+}/Cu^{2+}$ ratio, while the opposite is true for the apparent activation energy ($E_{app}$, kJ $mol^{-1}$). An $E_{app}$ of 80 kJ $mol^{-1}$ for $Cu^{+}/Cu^{2+} \sim 4.9$ compared to 125 kJ $mol^{-1}$ for $Cu^{+}/Cu^{2+} \sim 0.01$ was measured. $TOF_{CO}$ ($s^{-1}$) values were estimated based on the active sites associated with reaction intermediates truly participating in the CO oxidation reaction path. The $TOF_{CO}$ was also found to increase with increasing $Cu^{+}/Cu^{2+}$ ratio, largely due to the increased concentration of $Cu_2O$-CuO heterojunctions of the hollow structure formed ($Cu^{+}/Cu^{2+} \sim 4.9$), and likely to their enhanced site activity. Dynamic rates of lattice oxygen reduced and its amount (He → 1%CO/He step-gas switch) and those for oxygen refilling (He → 2% $O_2$/He step-gas switch) over the reduced $Cu_2O$-CuO, the chemical structures of CO-s and $CO_2$-s formed, and the thermal stability of $CO_2$-s in the oxygen atmosphere were determined. HRTEM highlighted the morphology change of $Cu_2O$ particles with varying calcination temperature of c-$Cu_2O$ NPs. X-ray photoelectron spectroscopy allowed us to estimate the surface $Cu^{+}$ and $Cu^{2+}$ composition as a function of calcination temperature. *In situ* CO-DRIFTS enabled the examination of variations in the surface $Cu^{+}/Cu^{2+}$ ratio under the CO oxidation reaction conditions.

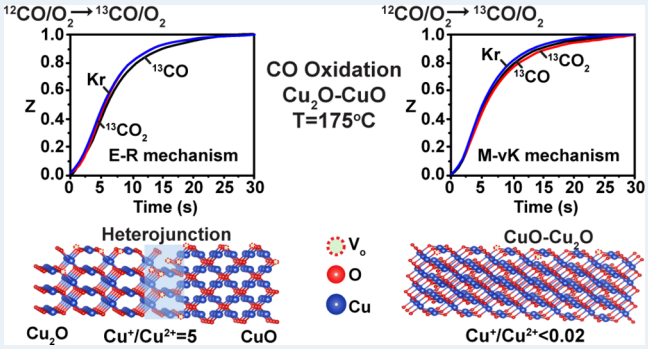


**KEYWORDS:** *SSITKA-CO oxidation, SSITKA-DRIFTS, $Cu_xO$, $Cu_2O$-CuO heterojunction, redox dynamics in $Cu_xO$, CO oxidation mechanism, reduction of lattice oxygen by CO*

## 1. INTRODUCTION

Catalytic CO oxidation (eq 1) has long played a pivotal role in the elimination of carbon monoxide in industrial flue gas streams and automotive exhausts and, recently, of traces CO in feed gas streams of fuel cells for proper operation.[1−6]

$$CO + \frac{1}{2}O_2 \rightarrow CO_2,\ \Delta H^{\circ} = -282\ \text{kJ mol}^{-1} \quad (1)$$

Received: September 22, 2025
Revised: February 16, 2026
Accepted: February 20, 2026
Published: March 9, 2026

Downloaded via UNIV OF LJUBLJANA on March 30, 2026 at 10:42:54 (UTC).
See https://pubs.acs.org/sharingguidelines for options on how to legitimately share published articles.

ACS Publications
© 2026 The Authors. Published by American Chemical Society



https://doi.org/10.1021/acscatal.5c06757
*ACS Catal.* 2026, 16, 5499−5519

The today's primary challenge in developing effective catalysts for CO oxidation is focused on the synthesis of cost-effective non-noble metal-based catalytic materials with high activity and stability.[6] Cu-based materials have attracted academic and industrial interest due to copper's high activity for CO oxidation, where copper is either anchored onto a metal oxide support (supported Cu) or introduced in its crystal structure (Cu-doped metal oxides).[6−13]

The catalytic performance of unsupported $Cu_xO$ ($x$ = 1 or 2) for CO oxidation is determined by variations in crystal structure and surface electronic characteristics that affect the chemisorption behavior of CO and $O_2$ (binding strength and surface coverage), as well as the offering of labile lattice oxygen.[14−16] Unsupported $Cu_2O$ was shown to exhibit complete oxidation of CO (3.6% CO/21% $O_2$/Ar) at room T for the first time,[17] while no significant conversion of CO had been observed at 140 °C over CuO.[18] On the other hand, $Cu_2O$-CuO heterojunctions ($Cu^+/Cu^{2+}$) formed after controlled calcination in air ($T_{calc}$ and time-on-stream) or *in situ* oxidation in $H_2O_2$ of pristine $Cu_2O$ were reported to exhibit high activity for CO oxidation at $T$ < 200 °C.[19−21] A $Cu_2O$-CuO heterojunction intermediate phase with increasing $T_{calc}$ was proposed according to Raman studies.[19] Due to the lattice mismatch at the interface of the heterojunction ($Cu_2O$-CuO) and coupled with the lattice strain, a large number of oxygen vacancies are formed as opposed to $Cu_2O$ and CuO (EPR studies). The sites at the interface are considered responsible for the high activity in the CO oxidation reaction.[21]

The complete CO conversion and stability at 150 °C in an $O_2$ rich environment (1% CO/20% $O_2/N_2$) were reported after optimization of the number density (per gram of material) of $Cu_2O$-CuO heterojunctions ($Cu^+/Cu^{2+}$ molar ratio).[19] This heterojunction in $Cu_xO$-$T_{calc}$ materials was proposed to synergistically promote the CO oxidation path by continuously generating and filling oxygen vacancies on the catalyst surface. The atomic-scale distance of $Cu_2O(Cu^+)$−$CuO(Cu^{2+})$ formed by the heterojunction was conducive to the rapid migration of oxygen formed after $O_2$ dissociation on $Cu_2O$ to fill an oxygen vacancy in CuO via oxygen spillover.[19] Similarly, Wei et al.[20] investigated the $Cu_2O$-CuO nanosphere system (hollow morphology) with a tunable $Cu^{2+}/Cu^+$ ratio for low-temperature CO oxidation (1% CO/3% $O_2/N_2$ gas mixture). Catalytic, kinetic, and characterization studies (TEM, XPS, FTIR, and $H_2$-TPR) resulted in a similar conclusion regarding the synergetic mechanism of the low-temperature CO oxidation: that $Cu_2O$ and CuO offer active sites for oxygen dissociation and CO oxidation, respectively. An optimum $Cu^{2+}/Cu^+$ molar ratio offers a matched reaction rate on the two solid domains for enhanced catalytic activity.[20] The hollow morphology for a given $Cu_2O$ or CuO nanoparticle size (nanometers) provides also a larger number of exposed copper ions at the surface and the interior cavity. A different chemical environment for specific $Cu_2O$ or CuO domains is formed, which was implied after comparing the CO oxidation activity between $Cu_2O$-CuO nanospheres and the milling mixture of $Cu_2O$/CuO nanospheres of similar size and chemical composition.[20]

Wang et al.[21] investigated the synergetic mechanism of $Cu^+$ and $Cu^{2+}$ double active sites present in the $Cu_2O$-CuO heterojunction (flower sphere nanoparticles) using $O_2$-TPD, *in situ* FTIR (CO/$O_2$ atmosphere), XPS, and DFT calculations. The main conclusions were that introducing CuO on the surface of $Cu_2O$ produces oxygen vacancies, new reaction sites, and two reaction paths at the interface. In the first path, CO and molecular $O_2$ are first adsorbed at the interface (heterojunction), and then, adsorbed molecular $O_2$ is activated and interacts with adsorbed CO to form $CO_2$; the RDS is that of the interaction between activated oxygen and adsorbed CO (Langmuir−Hinshelwood mechanism). The second path consists of the reaction between adsorbed molecular oxygen with CO(g) forming a chemical bond, followed by the spontaneous formation of $CO_2$(g) (Eley−Rideal mechanism). The first path with a lower barrier is favored at lower temperatures, while at higher temperatures, both reaction paths can occur.[21]

The identification of the contribution of different surface sites of c-$Cu_2O$ NCs in the catalytic activity of CO oxidation reaction (use of excess $O_2$ and up to 240 °C) was highlighted successfully by using large NCs (450−1030 nm), with face sites as the dominant active sites, and smaller NCs (34−110 nm) with edge sites.[22] During CO oxidation, a c-$Cu_2O$ (core)−CuO (shell) structure was evident (XRD, HRTEM, and XPS studies). Similar apparent activation energies $E_a$ of ∼120 kJ mol$^{-1}$ (Arrhenius plots) were estimated for the c-$Cu_2O$-CuO (450−1030 nm) system, as well as a much lower $E_a$ value of ∼80 kJ mol$^{-1}$ for the c-$Cu_2O$-CuO (34−110 nm) catalysts. The compensation effect in heterogeneous catalysis was also experienced.

Reaction kinetic analyses (examining the reaction orders of CO and $O_2$) and DFT calculations were conducted to investigate how site structure—specifically, face versus edge sites—impacts the mechanism of CO oxidation on c-$Cu_2O$-CuO catalytic surfaces.[22] For face sites on c-$Cu_2O$-CuO (450−1030 nm), the Mars−van Krevelen (M-vK) mechanism prevails: CO adsorbs at the $Cu_{3C}$ site, reacts with an adjacent $O_{3C}$ site to produce $CO_2$, and generates a surface oxygen vacancy ($O_v$). This reaction path displays a higher activation energy compared to that at step sites on c-$Cu_2O$-CuO (34−110 nm), where a L-H or M-vK mechanism prevails.[22]

CO oxidation on $Cu_2O$(111) was suggested to adopt the Eley−Rideal (E-R) mechanism, in which adsorbed oxygen species ($O_2$-s) react with CO directly from the gas phase,[23] while reaction with lattice oxygen has a higher energy barrier. Regarding the $Cu_2O$-CuO hollow nanosphere catalytic system with a tunable $Cu^+/Cu^{2+}$ ratio, Wei et al.[20] proposed the M-vK type mechanism that best explained the observed enhanced CO oxidation activity on $Cu_2O$-CuO composite structure. Dynamic studies on the kinetics and mechanism of reduction of $Cu_2O$ and CuO with CO and their dependence on morphology (the case of $Cu_2O$) were reported.[14,24] *In situ* synchrotron-based X-ray diffraction and EXAFS showed that the isothermal reduction mechanism can vary considerably with experimental conditions (e.g., gas flow-rate, CO concentration, and temperature), and complex kinetics must be involved.[14] The morphology-dependent reducibility of $Cu_2O$ NCs was also found to depend on the $P_{CO}$, where diffusion of subsurface lattice oxygen becomes a dominant process step with increasing $P_{CO}$.[24]

The present work was motivated by the lack of knowledge concerning the influence of the surface $Cu^+/Cu^{2+}$ molar ratio on the chemical composition and activity of the adsorbed phase formed on unsupported polycrystalline $Cu_2O$-CuO catalytic surfaces for the low-temperature CO oxidation in $O_2$-rich conditions. The influence of the $Cu^+/Cu^{2+}$ molar ratio on the mechanism of CO oxidation was also probed based on the analysis (material balances) of transient isotopic response


https://doi.org/10.1021/acscatal.5c06757
ACS Catal. 2026, 16, 5499−5519

curves of $^{13}CO$ and $^{13}CO_2$ after applying the steady state isotopic transient kinetic analysis ($^{12}CO/O_2 \rightarrow {}^{13}CO/O_2$ SSITKA step-gas switch) in combination with dynamic rate data analysis of the lattice oxygen reduction by CO. This novel methodology does not require the use of any DFT computations or microkinetic modeling. The composition of the active adsorbed phase and the mechanistic implications derived from the SSITKA response curves (mass spectrometry), and the recorded DRIFTS spectra of adsorbed reaction intermediates, reflected the intrinsic effects of the surface $Cu^+/Cu^{2+}$ molar ratio and not of any chemical composition alterations during CO oxidation. The latter appears to be a potential problem in common kinetic rate measurements by varying the partial pressures of the CO and $O_2$ and reaction temperature. The influence of the $Cu^+/Cu^{2+}$ ratio on the $TOF_{CO}$ ($s^{-1}$), which was estimated based on the concentration of active adsorbed CO-s and COO-s intermediates measured, is reported for the first time.

Following the establishment of a $Cu_2O/CuO$ (w/w) ratio and $Cu^+/Cu^{2+}$ surface molar ratio via *in situ* controlled calcination in 20% $O_2$/He on an initially synthesized c-$Cu_2O$ material, the reduction dynamics of $Cu_2O$-CuO by CO and subsequent reoxidation by $O_2$ were studied. High-resolution transmission electron microscopy (HRTEM), powder X-ray diffraction analysis (XRD/Rietveld), and ex situ X-ray photoelectron spectroscopy (XPS) were employed to characterize the morphology, bulk composition and primary crystallite size, and surface composition, respectively, of the $Cu_2O$-CuO heterogeneous nanocomposites as a function of the $Cu^+/Cu^{2+}$ molar ratio.

## 2. MATERIALS AND METHODS

### 2.1. Synthesis of $Cu_xO$-*T* Materials

Copper(II) acetylacetonate (0.130 g, 0.5 mmol) was mixed with octadecylamine (ODA, 0.80 g, 3 mmol) and 1-octadecene (ODE, 0.5 mL), and the resulting solution was then placed under vacuum at 120 °C for 1 h under $N_2$ gas for 10 min. Initially, the color of the solution at room temperature was blue, indicating the presence of cupric ions. As the temperature reached 120 °C, the solution turned dark green, most likely due to the formation of cuprous ions, and then yellow once it reached 200 °C. After maintaining the solution at 200 °C for 30 min, well-defined octahedral cuprite nanocrystals ($Cu_2O$-NCs) were observed.[25] For the cleaning process, acetone was added to the final solution, which was then centrifuged at 3500 rpm for 4 min. The precipitated solid particles were dispersed in chloroform and ethanol (added as an antisolvent). This cleaning procedure was repeated twice, followed by drying in a vacuum at 60 °C for 24 h and cooling to room temperature. The obtained sample is denoted as $Cu_xO$-RT.

The tuning of the $Cu^+/Cu^{2+}$ molar ratio in the as prepared $Cu_xO$-RT sample was achieved by adjusting the calcination temperature in the flow of a 20% $O_2$/He gas mixture. First, 100 mg of synthesized $Cu_2O$-RT sample was placed in a plug-flow quartz reactor and treated in $O_2$/He gas at 200 °C for 1 h (ramp heating rate of 5 °C $min^{-1}$). The sample was then cooled in an $O_2$/He gas flow to room T. This sample is denoted as $Cu_xO$-200. A second 100 mg sample was treated in $O_2$/He at 200 °C/1 h and then at 300 °C/1 h. At the end of this calcination process, the sample was cooled to room T in $O_2$/He. This sample is denoted as $Cu_xO$-300. A third 100 mg sample was treated at 200 °C/1 h, then to 300 °C/1 h, followed by another calcination treatment at 500 °C/1 h. At the end of this calcination process, the sample was cooled to room T in $O_2$/He. This sample is denoted as $Cu_xO$-500. Portions of these four $Cu_xO$-*T* samples (stored in vials after synthesis) were used for various characterizations as described in the following Section 2.2.

### 2.2. Characterization of $Cu_xO$-*T* Materials

The BET specific surface area (SSA, $m^2$ $g^{-1}$), total pore volume ($V_p$, $cm^3$ $g^{-1}$), and mean pore size ($d_p$, nm) of the $Cu_xO$-*T* materials were determined based on $N_2$ adsorption/desorption isotherms measured at liquid $N_2$ temperature (−196 °C) and using the Micromeritics Gemini 2360 surface area and pore size analyzer. Prior to any measurements, the samples were degassed in a $N_2$ gas flow at 200 °C for 3 h.

Powder XRD analysis was performed on a Panalytical XP PRO MPD apparatus using $Cu_{\alpha 1}$ irradiation ($\lambda$ = 1.5406 Å) in the 2theta range between 20 and 85°, step size of 0.017°, and fully opened 100 channel X'Celerator detector. Quantitative phase analysis was performed from Le Bail fit using the Topas Academic v.6 software package to estimate the mass fraction (wt %) of $Cu_2O$ and CuO in the $Cu_xO$-*T* solids.

Ex situ X-ray photoelectron spectroscopy (XPS) was used to identify the surface chemical composition and oxidation states of surface Cu and oxygen species in $Cu_xO$-*T* solids (Section 2.1). XPS measurements were performed using a Kratos Axis Ultra$^{DLD}$ spectrometer with a monochromatic AlK$\alpha$ X-ray source ($h\nu$ = 1486.6 eV) operated at 20 mA and 15 kV. Specimens were prepared by pressing a few milligrams of the sample in powder form onto an In substrate. Wide scans were collected over an analysis area of 300 × 700 $\mu m^2$ at a photoelectron pass energy of 160 eV (energy step of 1 eV), while high-resolution spectra were collected at a photoelectron pass energy of 20 eV and an energy step of 0.1 eV. Differential electrical surface charging effects in the samples were neutralized during the measurements by using the Kratos charge neutralizer system. The spectra obtained were analyzed with the CasaXPS software (Casa Software Ltd., version 2.3.24).[26]

The morphology of particles was observed using high-resolution transmission electron microscopy (Thermo Scientific Talos F200X). Samples were ground in agate mortar, dispersed in isopropanol, and dropped on a Cu-supported carbon film. A plasma cleaner was used to remove the organic contaminants. A crystallite size of 50 nm was used for simulations of the SAED data. Diffraction patterns of $Cu_2O$ and CuO were simulated using ICDD PDF-5+ software.

### 2.3. Steady State Kinetic Rate Measurements

The apparent activation energy ($E_a$, kJ $mol^{-1}$) of the CO oxidation reaction was estimated based on steady-state rate measurements of CO conversion ($\mu$mol CO $g^{-1}$ $s^{-1}$) versus the reaction temperature. The temperature ranges of 100−150 °C, 160−180 °C, and 170−200 °C were used, respectively, for the $Cu_xO$-200, $Cu_xO$-300, and $Cu_xO$-500 catalysts. A CSTR microreactor was used,[27] and the temperature of the catalyst sample was monitored by a K-type thermocouple in contact with the bottom of the catalytic bed. The rate of CO conversion and not that of $CO_2$ formation was used to avoid the possible influence of $CO_2$ readsorption. A reaction feed gas consisting of 1 vol % CO, 20 vol % $O_2$, and He as balance gas, a total flow rate, $F_T$ (50−100 N mL $min^{-1}$), and amounts of catalyst samples between 20 and 50 mg were used to keep the $Cu_2O/CuO$ mass ratio similar to that before reaction, the CO conversion below ca. 15%, and to minimize external and internal mass transport effects.[28] Steady-state kinetic rates were estimated after 30 min of CO/$O_2$/He gas flow over the fresh $Cu_xO$-*T* catalyst samples.

### 2.4. CO-Transient Isothermal Reduction (CO-TIR) Followed by Transient Isothermal Oxidation ($O_2$-TIO)

Transient isothermal reduction of $Cu_xO$-*T* solids by CO (CO-TIR) was conducted followed by transient isothermal oxidation ($O_2$-TIO) aiming to study the dynamics of their surface and subsurface lattice oxygen ($O_L$) reduction by CO(g) and reoxidation of the solid (refilling of the oxygen vacancies). The experimental apparatus used was previously described.[29] A 20 mg fresh sample ($Cu_xO$-*T*) was kept in place by quartz wool in the CSTR microreactor and first treated in 20% $O_2$/He at 150 °C for 30 min. The total volume flow rate of the feed gas stream was 50 NmL $min^{-1}$, and the temperature of the catalyst sample was monitored by a K-type thermocouple in contact with the bottom of the catalytic bed (exit of the product gas stream).


https://doi.org/10.1021/acscatal.5c06757
ACS Catal. 2026, 16, 5499−5519

The effluent gas stream from the reactor was continuously monitored by online mass spectrometry (QMS, Omnistar 1−300 amu, Balzer) for CO ($m/z$ = 28), $O_2$ ($m/z$ = 32), $CO_2$ ($m/z$ = 44), and Kr ($m/z$ = 84), followed by an infrared gas analyzer (Horiba, Model VA-3000) for CO and $CO_2$. Conversion of the MS and infrared CO/$CO_2$ analyzer signals to concentration (mol %) was performed using certified calibration gas mixtures (ca. 1 vol % CO/1 vol % $CO_2$/He, and 1 vol % $O_2$/He).

The experimental methodology of CO-TIR followed by $O_2$-TIO involved the following sequence of step-gas switches: He → 1 vol % CO/1 vol % Kr/Ar/He ($T$ = 175 or 190 °C, 15 min) → He (3 min) → 2 vol % $O_2$/1 vol % Kr/Ar/He ($T$ = 175 or 190 °C, 15 min). The dynamic rates ($\mu$mol $g^{-1}$ $s^{-1}$) of CO consumption (CO-TIR) and $O_2$ consumption ($O_2$-TIO) were calculated using eqs 2 and 3, respectively, while the amounts ($\mu$mol $g^{-1}$) of CO and $O_2$ consumed by integrating the respective dynamic rate response curves over time.

$$R_{CO}\ (\text{mol g}^{-1}\ \text{s}^{-1}) = \frac{F_T}{W} y_{CO}^{f} (Z_{Kr}(t) - Z_{CO}(t)) + NT\frac{dy_{CO}}{dt} \tag{2}$$

$$R_{O_2}\ (\text{mol g}^{-1}\ \text{s}^{-1}) = \frac{F_T}{W} y_{O_2}^{f} (Z_{Kr}(t) - Z_{O_2}(t)) + NT\frac{dy_{O_2}}{dt} \tag{3}$$

In eqs 2 and 3, $F_T$ denotes the feed gas stream's total molar flow rate (mol $s^{-1}$) and $y_{CO}$ is the CO mole fraction, with values of 1 vol % CO and 2 vol % $O_2$ as feed references. $N_T$ represents the total mol in the CSTR microreactor's gas phase, $W$ is the sample mass (∼ 0.02 g), and $Z_i$ is the normalized concentration of each gas (i = Kr, CO, $O_2$) relative to the feed value. The last term shown in eqs 2 and 3 was found to be negligible compared to the other components of the material balance and was thus omitted. The dynamic rates of $CO_2$ formation ($R_{CO2}$) were determined by analyzing the $CO_2$ response curve and applying a material balance similar to that in eq 2. These rates were then compared with those of $R_{CO}$.

The reproducibility of the CO-TIR followed by that of the $O_2$-TIO was checked by repeating this cycle twice in all three $Cu_xO$-$T$ samples. Following the 15 min oxidation step (2% $O_2$/Ar), the sample was maintained at either 175 or 190 °C for an additional 10 min, after which no further oxygen consumption was detected by the mass spectrometer. The timing, profiles, and characteristics of all recorded transient response curves were very much consistent, underscoring both the reliability of the experimental methodology and the reversibility of the redox cycle within the time frame of the redox experiment conducted.

## 2.5. Steady State Isotopic Transient Kinetic Analysis (SSITKA)-Mass Spectrometry

The carbon path of CO oxidation reaction at 175 °C was probed using steady state isotopic transient kinetic analysis coupled with mass spectrometry (SSITKA-MS),[30−32] aiming to estimate the following kinetic parameters for the working catalytic surface (under CO oxidation reaction conditions) of $Cu_xO$-$T$ solids; the SSITKA switch, 1 vol % **$^{12}$CO**/20 vol % $O_2$/He (175 °C, 30 min) → 1 vol % **$^{13}$CO**/20 vol % $O_2$/1 vol % Kr/Ar/He (175 °C, $t$), was performed.

1. The specific amount of reversibly chemisorbed CO-s established under reaction conditions ($N_{CO}$ ($\mu$mol $g^{-1}$)) was estimated using eq 4. The specific amount of active carbon-containing species present in the C-path ($N_{COO}$, mol $g^{-1}$) from the adsorbed CO-s (Langmuir−Hinshelwood and Mars−van Krevelen mechanisms) to the $CO_2$(g) was estimated using eq 5, while that in the case of an Eley−Rideal mechanism is followed via eq 6:

$$N_{CO}(\text{molg}_{cat}^{-1}) = \frac{F_T y_{CO}^{f}(1 - X_{CO})}{W} \int_0^{t^f} [Z_{Kr}(t) - Z_{^{13}CO}(t)]dt \tag{4}$$

$$N_{COO}(\text{molg}_{cat}^{-1}) = \frac{F_T y_{^{13}CO_2}}{W} \int_0^{t^f} [Z_{^{13}CO}(t) - Z_{^{13}CO_2}(t)]dt \tag{5}$$

$$N_{COO}(\text{molg}_{cat}^{-1}) = \frac{F_T y_{^{13}CO_2}}{W} \int_0^{t^f} [Z_{Kr}(t) - Z_{^{13}CO_2}(t)]dt \tag{6}$$

2. The mean residence time ($\tau_{CO}$, s) of the reversibly chemisorbed CO-s and that of the total active carbon-containing reaction intermediates, leading to $CO_2$(g), $\tau_{COO}$ (s), were estimated using eqs 7 and 8, respectively.

$$\tau_{CO}(s) = \int_0^{t^f} [Z_{Kr}(t) - Z_{^{13}CO}(t)]dt \tag{7}$$

$$\tau_{COO}(s) = \int_0^{t^f} [Z_{^{13}CO}(t) - Z_{^{13}CO_2}(t)]dt \tag{8}$$

3. The specific rate of CO conversion in terms of $TOF_{CO}$ ($s^{-1}$) was estimated based on the concentration of active adsorbed CO-s ($N_{CO}$) and COO-s ($N_{COO}$), and the specific kinetic rate, $R_{CO}$ (mol $g_{cat}^{-1}$ $s^{-1}$), was measured using eq 9. It should be noted that $N_{CO}$ is associated with the equivalent specific number (mol $g^{-1}$) of exposed surface $Cu^+$ and $Cu^{2+}$ sites to be discussed later.

$$TOF_{CO}(s^{-1}) = R_{CO}/(N_{CO} + N_{COO}) \tag{9}$$

In eqs 4−6, $F_T$ is the total feed molar flow rate (mol $s^{-1}$), $y_{CO}^{f}$ is the mole fraction of CO in the feed, $X_{CO}$ is the CO conversion (%), $W$ is the mass of catalyst (g), $y_{13CO2}$ is the mole fraction of $^{13}CO_2$ at the effluent gas stream of the microreactor in the new steady-state obtained under $^{13}CO/O_2$, $Z_i$ is the dimensionless concentration of a given gas-phase species i (i = Kr, $^{13}$CO, or $^{13}CO_2$), and $t^f$ is the time at which the new steady-state rate of $^{13}$CO conversion is obtained under $^{13}CO/O_2$. Two consecutive SSITKA switching experiments were performed, demonstrating that the transient response profiles for both $^{13}$C-labeled and unlabeled CO and $CO_2$ gases were consistently reproducible. The CO conversion was kept below 15% after adjusting the mass of the catalyst between 15 and 30 mg and the total volume flow rate of the feed gas stream to 50 NmL $min^{-1}$. The absence of external and internal mass transport resistances within the catalytic bed and individual catalyst particles was verified according to the methodology proposed elsewhere.[28] The mass numbers ($m/z$) 28, 29, 44, 45, 32, and 84 corresponding to $^{12}$CO, $^{13}$CO, $^{12}CO_2$, $^{13}CO_2$, $O_2$, and Kr were continuously monitored by online MS; the feed concentrations of CO and $O_2$ in the nonisotopic and isotopic feed gas mixtures were the same within 1%.

## 2.6. *In Situ* DRIFTS Studies

Diffuse reflectance infrared Fourier transform spectroscopy (DRIFTS) studies were conducted using a PerkinElmer Frontier FT-IR spectrometer equipped with a high-temperature/high-pressure temperature-controllable DRIFTS cell (Harrick, Praying Mantis, with the use of $CaF_2$ windows). The spectrometer settings were 256 scans per spectrum, the resolution was 4 $cm^{-1}$, and the scan speed was 2 cm $s^{-1}$ (MCT detector was used). The $Cu_xO$-RT catalyst sample (∼90 mg) before placing in the DRIFTS cell was ground and sieved into fine powder. The material was then calcined in place with 20% $O_2$/He at the same GHSV ($h^{-1}$), producing the $Cu_xO$-$T$ material described in Section 2.1.

**2.6.1. Probing Changes in the Surface $Cu^+/Cu^{2+}$ Distribution from Synthesis to CO Oxidation Reaction Conditions.** To investigate any changes in the $Cu^+/Cu^{2+}$ surface composition that may have taken place following the CO oxidation reaction (1% CO/20% $O_2$/He, 175 °C, 30 min) on the as-synthesized $Cu_xO$-$T$ solids (see Section 2.1), selective CO chemisorption at room temperature was used on $Cu^+$ and $Cu^{2+}$ sites according to the following


https://doi.org/10.1021/acscatal.5c06757
ACS Catal. 2026, 16, 5499−5519

experimental procedure. After placement of 95 mg of the synthesized $Cu_2O$ nanocrystals in the DRIFTS cell, the material was converted to $Cu_xO$-$T$ ($T$ = 200 or 500 °C) with specified $Cu_2O/CuO$ weight percent bulk composition (according to XRD) and surface $Cu^+/Cu^{2+}$ molar ratio (according to XPS), following the procedure outlined in Section 2.1. After cooling the solid in 20% $O_2$/He to room temperature, it was purged with a flow of He gas for 10 min before recording a DRIFTS background spectrum. Next, the solid was exposed to 1% CO/He for 30 min, after which a DRIFTS spectrum was collected. The solid was then exposed to 20% $O_2$/He and heated to 175 °C for 15 min, followed by exposure to 1% CO/20% $O_2$/He at 175 °C for 30 min. Afterward, it was flushed with He and allowed to cool to room temperature, and a background spectrum was recorded. Next, 1% CO/He was introduced for 30 min, after which a DRIFTS spectrum was recorded. The background spectrum recorded in flowing He at room temperature was subtracted from the spectrum obtained in flowing 1% CO/He.

Deconvolution and curve fitting of the DRIFTS spectra in the CO infrared region (covering both gaseous and adsorbed CO) were carried out according to the detailed methodology outlined in Section 3 of the SI. The integral band area ratio for adsorbed CO at room temperature associated with $Cu^+$ and $Cu^{2+}$ was subsequently determined, facilitating a comparative analysis between CO adsorption at room temperature before and after the CO oxidation reaction. Comparable values in the ratio indicate that the CO oxidation reaction conditions have resulted in minimal or no alteration of the surface $Cu^+/Cu^{2+}$ molar ratio relative to that observed in the fresh $Cu_xO$-$T$ solid.

**2.6.2. CO Oxidation Reaction Followed by Transient Isothermal Oxidation ($O_2$-TIO).** DRIFTS spectra were recorded under $CO/O_2$/Ar and $O_2$/Ar gas treatments following the sequence of step-gas switches: Ar (175 °C) → 1 vol % CO/20 vol % $O_2$/Ar (175 °C, 30 min) → 20 vol % $O_2$/Ar ($t$). The aim was to gather information about the reactivity toward oxygen of the various kinds of CO-s and other carbon-containing species (e.g., carbonate-type) formed after CO oxidation at 175 °C. The background DRIFTS spectrum of the solid was recorded in flowing Ar at 175 °C. This spectrum was then subtracted from the spectrum of the solid recorded in a $CO/O_2$/Ar or $O_2$/Ar gas mixture at 175 °C. Deconvolution and curve fitting procedures of the DRIFTS spectra in the CO IR region (gaseous and adsorbed CO-s) were performed as described in detail in the SI (Section 3). The DRIFTS spectra were smoothed when necessary to remove high-frequency noise and analyzed using Spectrum10 for Windows.

**2.6.3. Steady-State Isotopic Transient Kinetic Analysis (SSITKA-DRIFTS).** DRIFTS spectra were recorded before and after the SSITKA switch: 1 vol % $^{12}CO$/20 vol % $O_2$/Ar (175 °C, 30 min) → 1 vol % $^{13}CO$/20 vol % $O_2$/Ar (175 °C, 10 min). The obtained spectra were then subtracted from the background spectrum of the solid recorded in Ar at 175 °C. SSITKA-DRIFTS analysis was used to determine the chemical structure of adsorbed active reaction intermediates and those of inactive adsorbed species (spectators) formed during CO oxidation based on the red isotopic shift of relevant vibrational modes.[30,33,34] Details of the analysis of the CO IR region are reported in the SI (Section 3).

**2.6.4. $CO_2$ Chemisorption and Desorption in Ar Gas Flow.** The thermal stability of the adsorbed carbon dioxide product gas of the CO oxidation reaction in the form of carbonate-type species was investigated by time-resolved DRIFTS under Ar gas flow of the following step-gas switch: 1 vol % $CO_2$/Ar (175 °C, 30 min) → Ar (175 °C, $t$); a total volume flow rate of 50 NmL $min^{-1}$ was used.

## 3. RESULTS AND DISCUSSION

### 3.1. Surface and Bulk Characterization of $Cu_xO$-$T$ Materials

Figure 1A(a−d) displays the powder X-ray diffractograms recorded in a $N_2$ gas atmosphere at room T for the synthesized $Cu_xO$-$T$ catalysts following calcination at $T$ = 200, 300, and 500 °C, respectively, and before calcination (after vacuum

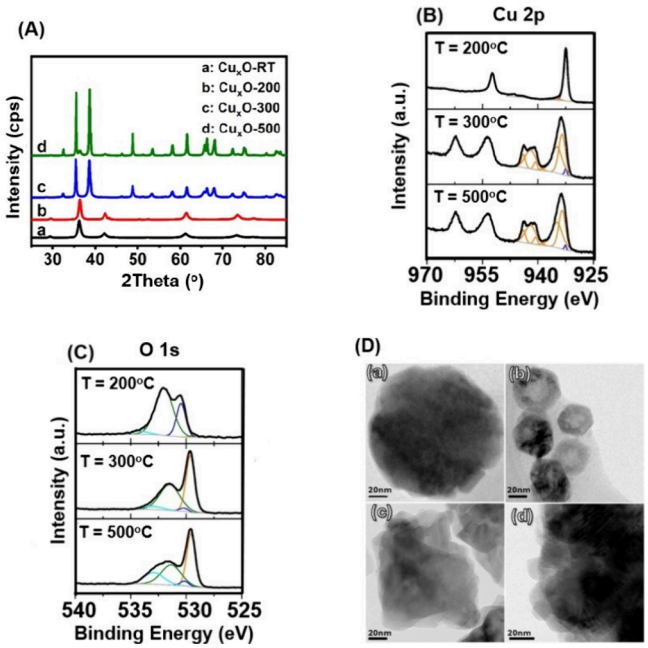


**Figure 1.** (A) Powder X-ray diffractograms of the $Cu_xO$-$T$ samples; (B) Cu 2p core-level spectrum (925−970 eV) and (C) O 1s core-level spectrum (525−540 eV) for the $Cu_xO$-$T$ samples after calcination at $T$ = 200, 300, and 500 °C; (D) bright-field TEM micrographs of the $Cu_xO$-RT (a), $Cu_xO$-200 (b), $Cu_xO$-300 (c), and $Cu_xO$-500 (d) samples.

drying; Figure 1A, a denoted as $Cu_xO$-RT). The sample before calcination is entirely composed of the octahedral phase of $Cu_2O$ (ICSD 9007497). The observed reflections at 2$\theta$: 29.36, 36.40, 42.10, 61.12, and 73.22° correspond to the (111), (200), (100), (220), and (311) planes, respectively. The average scattering domain size (crystal size) estimation resulted in an average $Cu_2O$ primary crystal size of $d_c$ ∼ 13 nm. After increasing the calcination T to 200 °C ($Cu_xO$-200), the only identifiable crystalline phase was that of $Cu_2O$ (Figure 1A, b), with the average crystal size increasing slightly to ∼16 nm. By further increasing the calcination temperature to 300 °C, the $Cu_xO$-200 solid was largely transformed into CuO ($Cu_2O + 1/2\ O_2 \rightarrow 2CuO$; ICSD 5000216) with the CuO phase consisting of primary crystals with an average size of $d_c$ ∼ 32 nm (Figure 1A, c; $Cu_xO$-300). A small fraction, ca. 0.2 wt % of $Cu_2O$, remained based on the Rietveld analysis performed. At the most intense calcination conditions applied (500 °C/1 h, $Cu_xO$-500 sample), the dominant phase remained that of CuO with an average crystal size almost twice as that estimated at 300 °C ($d_c$ ∼ 56 nm) and with $Cu_2O$ contributing to 3.9 wt % (Figure 1A, d; $Cu_xO$-500). The fact that the fraction of $Cu_2O$ increased relative to that at the lower calcination temperature of 300 °C is due to the sintering of $Cu_2O$ nanocrystals ($d_c$ < 4 nm, not seen by powder XRD). This result agrees with the XPS analyses, where surface $Cu^+$ was detected in the $Cu_xO$-300 and $Cu_xO$-500 samples but with a significantly lower $Cu^+/Cu^{2+}$ molar ratio as the calcination T increased to 500 °C.

Figure 1B, C shows the results of the ex situ XPS investigation on the $Cu_xO$-$T$ nanomaterials after calcination in 20% $O_2$/He gas flow at 200, 300, and 500 °C. The high-resolution scans obtained over the Cu 2p (Figure 1B) and O 1s (Figure 1C) regions are reported together with the results of the best fitting procedure applied for the quantification of


https://doi.org/10.1021/acscatal.5c06757
ACS Catal. 2026, 16, 5499−5519

surface Cu (different oxidation states) and O species as reported in Table 1. Analysis of the high-resolution Cu 2p peaks allows identifying the oxidation state of copper in the investigated samples.[35] The acquired data clearly indicate a change in the Cu oxidation state when the calcination temperature is brought to 300 °C and above. In fact, while the Cu 2p spectrum collected on the sample after calcination at 200 °C is characterized by the presence of two narrow peaks at ∼932.5 and ∼952.4 eV, the spectra collected on the samples calcined at higher temperatures show broader peaks and the presence of extra peaks in the 940−948 eV range and at ∼962.3 eV. The narrow peak at ∼932.5 eV observed on $Cu_xO$-200 could be either assigned to Cu(I) or Cu(0).[35] The inspection of the X-ray-induced Cu LMM Auger spectra (Figure S1, SI-Section 2) does allow for a more accurate assignment of these species.

**Table 1. Quantitative XPS Analysis of $Cu^+$ and $Cu^{2+}$ Oxidation States in $Cu_xO$-*T* Solids**

| catalyst | $Cu^+$ (%) | $Cu^{2+}$ (%) | $O_L$ ($Cu_2O$), % | $O_L$ (CuO), % |
|---|---|---|---|---|
| $Cu_xO$-200 | 83.0 ± 1.5 | 17.0 ± 2.6 | 94.4 ± 1.2 | 5.6 ± 0.5 |
| $Cu_xO$-300 | 2.5 ± 0.5 | 97.5 ± 0.5 | 5.5 ± 1.4 | 94.5 ± 0.8 |
| $Cu_xO$-500 | 1.0 ± 0.5 | 99.0 ± 0.5 | 7.4 ± 1.5 | 92.6 ± 1.3 |

The main Cu LMM Auger peak at 916−917 eV and the lack of a peak at 918.6 eV indicate that no Cu(0) is present, supporting assignment of the narrow Cu 2p XPS peak at 932.5 eV to Cu(I) in $Cu_2O$.[35] The appearance of satellite peaks in the 940−948 eV range in the data collected on $Cu_xO$-300 and $Cu_xO$-500 samples is indicative of the presence of Cu(II).[35,36] The shape of these satellite peaks together with the components at 934−935 eV (orange profiles in Figure 1B) is consistent with the presence of CuO.[35,36] The XPS area of the Cu 2p components can be used to estimate the $Cu^+$ and $Cu^{2+}$ at. % composition and therefore the $Cu^+/Cu^{2+}$ molar ratio in the samples. The reported values (Table 1) were calculated, assuming a homogeneous distribution of the oxidation states within the top atomic layers (up to ∼5 nm depth) in the samples. The $Cu^+$ composition (at. %) and $Cu^+/Cu^{2+}$ surface ratio show a significant decrease from 200 to 500 °C, a calcination temperature at which the $Cu^+$ content is reduced to ∼1.0 at. % of the total surface Cu seen by XPS.

The presence of both $Cu^+$ and $Cu^{2+}$ oxidation states is further confirmed by analysis of the O 1s XPS signal. Indeed, the spectra collected on the samples after calcination (Figure 1C) showed narrow peaks at ∼530 eV, together with signals at a higher binding energy. The high-energy signals arise from adsorbed oxygen species ($O_{ad}$), hydroxyl groups (OH), and carbonate-type species, which are commonly observed on the surface of calcined metal oxides after synthesis and exposure to air.[36] The signal at low binding energy can be decomposed into two peaks, one at 529.7 ± 0.2 eV, typical of CuO, and one at 530.2 ± 0.2 eV, in line with literature reports for $Cu_2O$.[35] Their concentration ratio evolves with increasing calcination temperature, in line with the Cu 2p XPS data. This behavior further confirms the thermal oxidation of $Cu^+$ to $Cu^{2+}$ as the calcination temperature increases. In the current ex situ XPS measurements, exposure of the $Cu_xO$-*T* samples to ambient air prevents definitive conclusions from being drawn about variations in adsorbed oxygen ($O_{ad}$) as a function of the $Cu^+/Cu^{2+}$ molar ratio.

In the case of the $Cu_xO$-200 sample, the relative atomic fractions of the two copper oxidation states are 83% and 17%, for $Cu^+$ and $Cu^{2+}$, respectively. Assuming that these oxidation states correspond exclusively to $Cu_2O$ and CuO, the surface lattice oxygen ($O_L$) distribution in the $Cu_2O$ and CuO system is estimated to be ∼71 and ∼29%, respectively. The %-deviation between the $O_L$ distribution determined by XPS (Table 1) and the estimated value appears to be ∼25% for the $O_L$ in the $Cu_2O$ system. On the other hand, the relatively low CuO content inferred for the $Cu_xO$-200 sample suggests the possible presence of surface $Cu^{2+}$ species other than CuO, likely surface hydroxylated/carbonated $Cu^{2+}$ species (ex situ XPS). These species would contribute to the $Cu^{2+}$-related signal in the Cu 2p region while contributing to the high binding energy side of the O 1s spectrum. Indeed, the reported O 1s binding energies for $Cu(OH)_2$ and $CuCO_3$ are 530.85 and 530.95 eV, respectively, which could lead to a wrong estimation of the CuO contribution.[37] Furthermore, the presence of amorphous CuO would result in a broadening of the related O 1s signal. Given the presence of heterojunctions in the $Cu_xO$-200 sample to be discussed later, the precise separation of the two O 1s contributions would be inherently uncertain, and small changes in, for example, FWHM constraints in the fitting procedure, would alter the analysis. It should be noted that XRD measurements did not detect any crystalline CuO phase (Figure 1A, b). This suggests that there could be an amorphous form of CuO present or perhaps thin layers of amorphous CuO coating the original $Cu_2O$ particles. Recent studies have noted that understanding defects caused by oxygen vacancies or interstitial species in amorphous oxides is still challenging. This is mainly due to the lack of long-range order and wide variations in local atomic environments, which alter local Cu:O stoichiometries.[38] Overall, all the above-mentioned factors might explain the larger deviation observed for the $O_L$ component attributed to CuO, compared to $Cu_2O$, between the value reported in Table 1 and that estimated from the $Cu^+/Cu^{2+}$ ratio.

The HRTEM images of $Cu_xO$-*T* samples are shown at a higher magnification in Figure 1D and at lower magnification with included SAED patterns in Figure S2. The $Cu_xO$-RT sample consists of polyhedral particles of a wide distribution, ca. 50−300 nm, where the SAED pattern obtained from several particles shows only rings characteristic of c-$Cu_2O$ (Figure S2a). Rings are not continuous but slightly speckled, indicating the random orientation of crystallites. A similar SAED pattern was obtained on the edge of individual large particles, indicating that the $Cu_2O$ particles are composed of smaller, closely stacked primary nanocrystallites.

As the calcination temperature increased to 200 °C ($Cu_xO$-200 sample), the formation of voids (Figure 1D(b)) is clearly observed, as opposed to the case of the $Cu_xO$-RT sample (Figure 1D(a)). Unequal diffusion rates of copper and oxygen ions upon mild sample calcination (ca. 200 °C/1 h) caused outward diffusion of $Cu^+$ ions toward a layer of CuO-$Cu_2O$ to continue the oxidation process.[20] This mass transport process led to the formation of voids in the particles. This effect was also observed (HRTEM) and reported by Susman et al.[39] on Cu NPs after oxidation in air at 155 °C. The authors proposed that this is a manifestation of the Nano Kirkendall Effect (NKE), an atomic interdiffusion at the interface of two metals through a vacancy exchange mechanism, which described very well the formation of hollow interiors in the reacting copper solid nanoparticles. Wei et al.[20] reported the formation of


https://doi.org/10.1021/acscatal.5c06757
ACS Catal. 2026, 16, 5499−5519

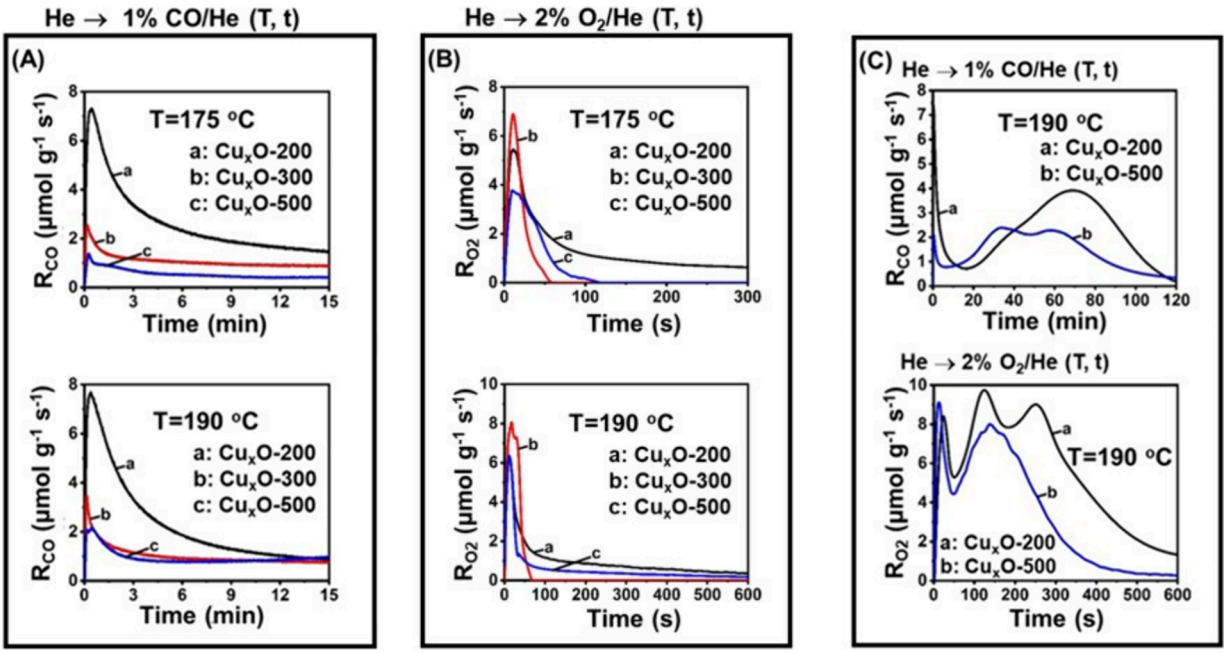


**Figure 2.** (A) Dynamic rate ($\mu$mol g$^{-1}$ s$^{-1}$) response curves of CO conversion after the switch He → 1% CO/He ($T$, $t$) at $T$ = 175 and 190 °C, $t$ = 15 min; (B) dynamic rate ($\mu$mol g$^{-1}$ s$^{-1}$) response curves of $O_2$ consumption obtained at the last switch of the following sequence of step-gas switches over the $Cu_xO$-$T$ catalytic samples: He → 1% CO/He ($T$, $\Delta t$) → He (5 min) → 2% $O_2$/He ($T$, $t$); $T$ = 175 and 190 °C, $\Delta t$ = 15 min, $t$ = 15 min; (C) dynamic rate ($\mu$mol g$^{-1}$ s$^{-1}$) response curves of CO conversion and $O_2$ consumption obtained according to the above step-gas switches over the $Cu_xO$-200 and $Cu_xO$-500 samples at $T$ = 190 °C, $\Delta T$ = 2 h, and $t$ = 15 min.

hollow nanospheres of similar structure but of different $Cu^+$/$Cu^{2+}$ molar ratio after increasing the calcination temperature from 260 to 300 °C in air in the case of $Cu_2O$ nanoparticles.

By further increasing the calcination temperature to 300 °C ($Cu_xO$-300, Figure 1D(c)), the morphology changed significantly. If $Cu_xO$-RT and $Cu_xO$-200 could be identified as cube-like or polyhedron-like nanoparticles (Figure S2a−b), the $Cu_xO$-300 consists of shapeless particles of a broad size distribution (ca. 30−200 nm, Figure S2c). The SAED pattern consists of faint speckled rings characteristic of $Cu_2O$, a clearly visible speckled ring pattern, and individual bright spots corresponding to monoclinic CuO. Rietveld refinement of the powder XRD profile (Figure 1A, c) identified CuO as the dominant crystalline phase in this $Cu_xO$-300 sample, revealing almost complete transformation of $Cu_2O$ to CuO. The observed structural evolution is consistent with thermal sintering and formation of the thermodynamically most stable phase of CuO. The gradual transformation of $Cu_2O$ to CuO as the calcination temperature increased accompanied by morphology changes was also reported by Chang et al.[40] in their study on the effect of calcination-induced oxidation of $Cu_2O$ (nanocube morphology) on the photocatalytic $H_2$ production performance of $Cu_2O$-CuO composite materials. Sample $Cu_xO$-500 with a similar phase composition to that of $Cu_xO$-300 consists of larger CuO particles, ca. larger than 300 nm (Figure S2d). The SAED pattern shows similar characteristics, suggesting that the large particles observed are indeed agglomeration of closely packed crystals of smaller size. CuO is the dominant crystalline phase, as previously mentioned and discussed. We should also note that the hollow structure of $Cu_xO$-200 solid (Figure 1D, b) was hardly seen in the $Cu_xO$-300 and $Cu_xO$-500 solids. Overall, the evolution of the $Cu^+$/$Cu^{2+}$ ratio (XPS study) illustrates the transformation of $Cu_2O$ to CuO along with significant changes in NP morphology (Figure 1D and Figure S2, HRTEM).

The BET surface areas of $Cu_xO$-$T$ solids were found to be ∼4, 12, 13, and 16 m$^2$ g$^{-1}$, respectively, for room T and after calcination at 200, 300, and 500 °C. Also, the specific total pore volumes ($V_p$) were found to be 0.005, 0.045, 0.024, and 0.020 cm$^3$ g$^{-1}$, respectively. The $N_2$ adsorption/desorption isotherms obtained at 77 K for the $Cu_xO$-$T$ solids are reported in Figure S3A−D, which are characterized as H3-type for the $Cu_xO$-room T sample and H4-type for the samples calcined at 200, 300, and 500 °C.[41] It is seen that the increase of calcination T from 200 to 500 °C resulted in an ∼35% increase of BET area, and this result is linked to the clear morphological changes induced by the calcination T (see HRTEM, Figure 1D).

Given the characterization results for the $Cu_xO$-$T$ solids and the preceding discussion, it is useful to summarize the key features of these structures, as they are likely to influence the different kinetic behaviors discussed later. As $Cu_2O$ NPs were calcined in a 20% $O_2$/He gas mixture at 200 °C/1 h, unique hollow structures of cube- and polyhedron-like shape of an average primary crystal size of $d_c$ ∼ 16 nm were formed, consisting of $Cu_2O$ (core) and CuO on top with 17 at. % $Cu^{2+}$ surface composition. Detailed analysis of the structure of this CuO material formed and the resulting interface with $Cu_2O$ nanocrystals (heterojunction) was not performed. However, evidence from the XPS results allows us to suggest that amorphous CuO is likely to have been formed on top of $Cu_2O$ (core). The formation of voids (hollow structures) indicates the development of new interior heterojunctions, as oxygen gas can diffuse through these voids and facilitate the transformation of $Cu_2O$ to CuO. The existence of such heterojunctions suggests the generation of oxygen vacancies


https://doi.org/10.1021/acscatal.5c06757
ACS Catal. 2026, 16, 5499−5519

**Table 2. Maximum Dynamic Rates ($R_o$) of CO and $O_2$ Consumption, Time of Their Appearance ($t_{max}$), and Amounts (mmol O $g^{-1}$) of Oxygen Reduced and Consumed According to the CO-TIR ($\Delta t$ = 15 min) and $O_2$-TIO (15 min) Sequence of Step-Gas Switches Applied over the $Cu_xO$-*T* Samples**

| | | *T* = 175 °C | | | *T* = 190 °C | | |
|---|---|---|---|---|---|---|---|
| catalyst | gas switch | $R_o$ ($\mu$mol $g^{-1}$ $s^{-1}$) | $t_{max}$ (s) | $N_o$ (mmol O $g^{-1}$) | $R_o$ ($\mu$mol $g^{-1}$ $s^{-1}$) | $t_{max}$ (s) | $N_o$ (mmol O $g^{-1}$) |
| $Cu_xO$-200 | He → CO/He | 7.3 | 26 | 2.36 (9.8)[a] | 7.7 | 23 | 2.04 (8.5)[a] |
| | He → $O_2$/He | 5.5 | 11.0 | 1.1 | 6.2 | 12.4 | 1.18 |
| $Cu_xO$-300 | He → CO/He | 2.5 | 10 | 0.97 (2.6)[a] | 3.5 | 8 | 0.92 (2.4)[a] |
| | He → $O_2$/He | 6.9 | 10.9 | 0.30 | 8.1 | 17.4 | 0.58 |
| $Cu_xO$-500 | He → CO/He | 1.4 | 18 | 0.50 (1.3)[a] | 2.2 | 23 | 0.86 (2.2)[a] |
| | He → $O_2$/He | 3.8 | 10.4 | 0.33 | 9.1 | 11.4 | 0.33 |

[a] $N_{O,m}$ = equivalent number of surface oxygen monolayers.

($V_O$), a phenomenon that is well-documented in the literature concerning comparable unsupported $Cu_2O$-CuO systems.

In the case of the $Cu_xO$-300 solid, almost complete transformation of the original $Cu_2O$ single phase to CuO (97.5 at. % surface $Cu^{2+}$) occurred, consisting of larger primary crystallites (average $d_c$ ~ 32 nm) and large particles (30−200 nm) due to thermal agglomeration. It appears also that these large crystals do not exhibit a hollow structure. The small $Cu^+$ surface concentration detected should be interpreted as due to the outward $Cu^+$ diffusion during the transformation of $Cu_2O$ to CuO, which could not get oxidized to $Cu^{2+}$ for the calcination conditions applied. This $Cu_xO$-300 system must obviously have only a small concentration of heterojunctions. In the case of the $Cu_xO$-500 solid, further calcination to 500 °C/1 h resulted in a solid with 99 at. % $Cu^{2+}$, larger primary crystals (avg. $d_c$ of ~56 nm), and particles (agglomerates) larger than 300 nm. The main reason for the expected differences in the upcoming kinetic experiments between $Cu_xO$-300 and $Cu_xO$-500 solids is believed to be the variation in the average primary crystal size of the CuO phase in the two solids, as well as the approximately 2.5-fold difference in surface $Cu^+$ content (Table 1). The latter could be linked to the formation of heterojunctions and other surface defects.

### 3.2. Transient Kinetics of $Cu_2O$-T Reduction by CO

**3.2.1. Dynamics of Lattice Oxygen Reduction by CO - Mass Spectrometry Analysis.** Figure 2A presents the dynamic rate profiles of CO consumption ($R_{CO}$, $\mu$mol $g^{-1}$ $s^{-1}$) obtained during the step-gas switch He → 1 vol % CO/He (*t*) conducted at 175 and 190 °C over the three $Cu_xO$-*T* catalysts for 15 min in CO/He. The initial sharp increase in the $R_{CO}$ upon the switch to CO/He is due to the reaction of CO with surface lattice oxygen ($O_{Ls}$) forming $CO_2$(g) and leaving behind an oxygen vacancy ($V_O$). The rather slow decay following the peak maximum in $R_{CO}$ and the tail that developed after ~5 min of reaction are attributed to the reaction of CO with subsurface (bulk) lattice oxygen, $O_{Lb}$. Oxygen vacancies ($V_O$) promote the diffusion of $O_{Lb}$ to the surface (activated process), thereby affecting the kinetics of CO oxidation by $O_{Ls}$. The reaction between CO and $O_{Ls}$ to yield $CO_2$ is described by eq 10, which involves adsorbed CO-s. Subsequent *in situ* DRIFTS investigations have confirmed this, as will be discussed further below.

$$\text{CO-s} + O_{Ls} \rightarrow CO_2(g) + \text{Vo} \quad (10)$$

Among the three investigated solids, $Cu_xO$-200 exhibits the largest rate of CO consumption at the very initial period of the transient ($R_o$, maximum rate value) at both 175 and 190 °C. At 175 °C, the $R_o$ for the $Cu_xO$-200 solid is 2.9- and 5.2-times higher compared to those for $Cu_xO$-300 and $Cu_xO$-500 solids, respectively (Figure 2A upper graph, Table 2), while at 190 °C, it is 2.2- and 3.5-times higher (Figure 2A lower graph, Table 2). Additionally, the time of appearance of $R_o$, $t_M$ (s), for the $Cu_xO$-200 sample occurs at longer times (ca. $t_M$ = 26 s) compared to those for $Cu_xO$-300 ($t_M$ = 10 s) and $Cu_xO$-500 ($t_M$ = 18 s) solids. The activity of the solids in terms of the amount of lattice oxygen removed, $N_O$ (mmol O $g^{-1}$), after 15 min of exposure to the 1% CO/He gas mixture, follows the order $Cu_xO$-200 > $Cu_xO$-300 > $Cu_xO$-500 (Table 2). For the $Cu_xO$-200 most active solid in CO oxidation, 2.36 and 2.04 mmol of O $g^{-1}$ were removed at 175 and 190 °C, respectively, while in the case of the least active $Cu_xO$-500 solid, 0.50 and 0.86 mmol of O $g^{-1}$ were removed at 175 and 190 °C, respectively. In other words, in the case of $Cu_xO$-200 ($Cu^+$/$Cu^{2+}$ ratio of ~5.0), 4.7- and 2.4-times larger amounts of lattice oxygen reacted with CO at 175 and 190 °C, respectively, compared to the $Cu_xO$-500 sample ($Cu^+$/$Cu^{2+}$ ratio of ~0.01). After considering the crystallographic data for the number density of oxygen atoms (O atoms/$nm^2$) in the case of most stable $Cu_2O$(111) and CuO(111) facets, the BET area, and the XPS composition of $Cu_xO$-*T* samples, the equivalent number of surface lattice oxygen monolayers ($N_{O,m}$) reduced by CO in the $Cu_xO$-*T* solids can be provided. In the case of $Cu_xO$-200, one surface oxygen monolayer was estimated to be ~0.24 mmol of O $g^{-1}$, thus providing $N_{O,m}$ ~ 10 monolayers of lattice oxygen reduced at 175 °C. In the case of $Cu_xO$-500, one surface oxygen monolayer was estimated to be 0.383 mmol of O $g^{-1}$, resulting in $N_{O,m}$ ~ 1.3.

Given the $Cu_2O$(111) *d*-spacing of 0.24 nm and XPS's ~5 nm analysis depth, the $Cu^+$/$Cu^{2+}$ molar ratios reported in Table 1 represent the surface composition of the first 20−25 atomic layers of $Cu_xO$-*T* samples. Thus, the observed surface and subsurface oxygen reduction dynamics (Figure 2A) and $N_{o,m}$ values (Table 2) directly relate to the surface structure previously discussed. Considering the $N_{o,m}$ values for each solid (corresponding to the 15 min CO/He treatment) and the time development of $R_{CO}$ response curves (Figure 2A), it can be identified that the $Cu_xO$-200 solid shows faster subsurface oxygen ($O_{Lb}$) diffusion rates toward the surface than the other two solids. Undoubtedly, $R_o$ values refer to reduction rates of surface lattice oxygen ($O_{Ls}$), where the $Cu_xO$-200 solid also shows significantly higher reduction rates as previously discussed. Considering the hollow structure of $Cu_xO$-200 particles (Figure 1D, b) and the relative discussion offered previously, the significantly higher $R_o$ values exhibited by this sample are likely to largely reflect the presence of labile surface lattice oxygen linked with the $Cu^+$−O−$Cu^{2+}$ heterojunction surface sites. In fact, the significant effect of the heterojunction


https://doi.org/10.1021/acscatal.5c06757
ACS Catal. 2026, 16, 5499−5519

interface's contribution in the CO oxidation reaction for the $Cu_2O$-CuO system of varying surface $Cu^+/Cu^{2+}$ molar ratios was systematically investigated by Shi et al.[19] Raman and $H_2$-TPR studies provided evidence for the presence of a heterojunction intermediate phase, and reduction traces appeared at lower temperatures compared to the pristine $Cu_2O$ and CuO phases.

For longer reaction times in 1% CO/He (ca. 2 h) and for the higher temperature used (190 °C), the developed dynamics of lattice oxygen reduction by CO was largely different (Figure 2C, upper graph) when compared to the case of short reduction times (ca. 15 min, Figure 2A). The interest here is to show characteristics of the dynamic reduction of subsurface/bulk lattice oxygen in the solid structure by CO, where bulk oxygen diffusion toward the surface prevails. Of particular interest was to compare the two different morphologies, the hollow $Cu_2O$ NCs (core)/CuO (deposits) [$Cu_xO$-200 sample] and that of significantly larger CuO NCs (99 at. % $Cu^{2+}$) [$Cu_xO$-500] (see Figure 1D). In the case of $Cu_xO$-200, a large peak of $R_{CO}$ appeared after ∼70 min with a shoulder at a lower reaction time (∼30 min), where in the case of $Cu_xO$-500, two clear peak maxima at similar reaction times were observed (Figure 2C, upper graph/curve b). The amount of lattice oxygen reduced by CO was found to be larger by ∼1.4-times in the case of $Cu_2O$-200 compared to $Cu_xO$-500, a result similar to that seen for short reaction times (Table 2). It should be noted that very similar dynamic response curves were obtained for the $CO_2$ formation, where the equivalent amounts of $CO_2$ formed were within 7% of those reported for the CO consumption. This result shows that the amount of adsorbed CO-s and likely $CO_2$-s (after $CO_2$ readsorption) during the dynamic reduction of $Cu_xO$-*T* solids by CO was small; thus, the $R_{CO}$ practically corresponds to the dynamic rate of CO oxidation by lattice oxygen to $CO_2$(g).

These different dynamic features in the reduction of $Cu_xO$-*T* by CO at 175 and 190 °C are closely related to the different surface chemical compositions, structures (surface/bulk), and morphologies of the three solids as previously discussed. In the present work, the initially formed $Cu_2O$-RT NPs after mild calcination in air at 200 °C/1 h produced a layer/patches of CuO onto a defective $Cu_2O$ structure and voids in the initial $Cu_2O$ particles. As stated earlier, CuO-$Cu_2O$ heterojunctions are formed with a new local coordination environment for oxygen and copper atoms.[20] This new surface structure must be considered to significantly contribute in the reduction of lattice oxygen of $Cu_xO$-200 (outside and in the interior of hollow NCs) and, to a lesser extent, in the case of $Cu_xO$-300 and $Cu_xO$-500 solids (a small fraction of the $Cu_2O$ phase is present). In all cases (Figure 2A, C/upper graph), the $Cu_xO$-200 sample presented higher activity in terms of the total amount of lattice oxygen reduced ($N_O$, mmol of O $g^{-1}$) as reported in Table 2. Wang et al.[21] have investigated CuO/$Cu_2O$ heterojunction catalytic systems for low-temperature CO oxidation. An optimum surface $Cu^{2+}/Cu^+$ ∼ 1 (XPS studies) interface sites, a large concentration of oxygen vacancies ($O_{vs}$, EPR studies), and low-T reducible $Cu^+/Cu^{2+}$ sites ($H_2$-TPR studies) were reported, after oxidation of $Cu_2O$ nanospheres in $H_2O_2$ solution, all being critical parameters responsible for the best CO oxidation activity obtained.

Based on DFT computations,[15] the energy barrier of oxygen vacancy formation ($E_{O\text{-}vac}$) for CuO(111) was found to be larger than that for $Cu_2O$(111). Hence, the formation of oxygen vacancies in CuO is thermodynamically less favored compared to $Cu_2O$, and similarly the kinetic rate of subsurface oxygen diffusion ($O_{Lb}$) toward the surface. In the case of the $Cu_xO$-200 solid, where the $Cu_2O$ phase is clearly present (Figure 1A, b), reduction of oxygen located at the $Cu^+$−O−$Cu^+$ sites by CO partly contributes to the larger quantities of lattice oxygen removed from the $Cu_xO$-200 compared to $Cu_xO$-300 and $Cu_xO$-500 solids (Table 2). The higher concentration of oxygen vacancies present in $Cu_2O$ is expected to enhance the diffusion of subsurface lattice oxygen toward the surface for reaction with CO as reaction is progressing. This result partly explains the higher rates exhibited by $Cu_xO$-200 compared to $Cu_xO$-500 for longer times in the CO/He reaction gas at 190 °C (ca. 40−120 min range; Figure 2C/upper graph).

**3.2.2. Dynamic Oxidation of Prereduced $Cu_xO$-*T* Solids.** The dynamic isothermal rate response curves of $O_2$ consumption, $R_{O2}$ ($\mu$mol $g^{-1}$ $s^{-1}$), obtained over the prereduced $Cu_xO$-*T* samples, after following 15 min of CO isothermal reduction (CO-TIR) (Figure 2A) and a 5 min He purge, are depicted in Figure 2B. The amount of $O_2$ consumed $N_O$ (mmol $g^{-1}$) after 15 min in $O_2$/He was estimated after integrating the $R_{O2}$ over this period, and the results are reported in Table 2. The dynamic $R_{O2}$ rate profiles reflect the different kinetics followed for oxygen refilling both the surface and bulk oxygen vacant sites $V_O$ that were formed during the CO reduction step. The concentration and nature of these $V_O$ sites depend on the structure of $Cu_xO$-*T*, as well as the temperature and time on stream under the preceding CO reduction step (see Table 2, $N_o$ quantity under He → $O_2$/He). It is interesting to note that larger initial rates of reoxidation (ca. $t$ < 30 s) are seen for the solids with very large concentrations of $Cu^{2+}$ (very low $Cu^+/Cu^{2+}$ molar ratio, Table 1) compared to the $Cu_xO$-200 sample (low $Cu^{2+}$ concentration), as opposed to the CO reduction step (compare Figure 2A and Figure 2B). This result finds support by the fact that the higher the energy for the $V_O$ formation, the more facile the lattice oxygen refilling when set in contact with the oxygen gas atmosphere.[15]

Largely different dynamic isothermal $R_{O2}$ response curves were obtained following longer reduction times ($\Delta t$ = 2 h) in CO/He at 190 °C in the case of $Cu_xO$-200 and $Cu_xO$-500 solids (Figure 2C/lower graph). Multiple rate maxima appear ($Cu_xO$-200: $t_M$ = 24, 126, 251 s; $Cu_xO$-500: $t_M$ = 13, 140 s), which highlight the rather complex mechanism of reoxidation of the reduced $Cu_xO$ phases, or equivalently the refilling of the oxygen vacant sites created after the CO reduction step. The dynamics of reoxidation of partly reduced $Cu_2O$ ($Cu^+/Cu^\circ$) and CuO ($Cu^{2+}/Cu^+$) must depend on the surface and bulk structure of $Cu_2O$/CuO and the nature of specific heterojunctions formed at the interface of reduced $Cu_2O$-core/CuO in $Cu_xO$-*T* following the CO/He gas treatment. This would affect surface/bulk oxygen diffusion barriers in the two systems. The amounts of oxygen consumption $N_O$ (after 15 min in $O_2$/He) were found to be 9.2 and 4.03 mmol of O $g^{-1}$ for the $Cu_xO$-200 and $Cu_xO$-500 solids, respectively. It is interesting to compare this oxygen consumption (refilling of $V_O$) after 15 min in 2% $O_2$/He with the amount of lattice oxygen removed after 2 h of reduction of the solids in 1% CO/He (Figure 2C/upper graph). It is seen that ∼90% and 56% of oxygen reduced were restored for the $Cu_xO$-200 and $Cu_xO$-500 catalysts, respectively. This result highlights again the faster diffusion of oxygen in the lattice of $Cu_xO$-200 ($Cu_2O$-CuO heterojunctions) than in $Cu_xO$-500 (practically CuO


https://doi.org/10.1021/acscatal.5c06757
ACS Catal. 2026, 16, 5499−5519

phase) solid systems. The observation of three rate maxima in the dynamics of oxygen uptake by the reduced $Cu_xO$-200 sample at 190 °C/2 h (Figure 2C/lower graph, curve a) illustrates the fast refilling of surface oxygen vacant sites[21] followed by the oxidation of reduced CuO initially formed on top of $Cu_2O$, followed by the refilling of subsurface $V_O$ via oxygen bulk diffusion; several monolayers of O were removed after reduction of $Cu_xO$-*T* by CO as reported in Table 2.

**3.2.3. *In Situ* DRIFTS.** In order to provide information on the structure of adsorbed CO-s on the $Cu^+$ and $Cu^{2+}$ surface sites and their relative surface concentration related to the dynamics of the reduction of $Cu_xO$-*T* solids by gaseous CO at 175 °C, *in situ* DRIFTS spectra were recorded after the solids were exposed to a 1% $^{12}CO$/He gas mixture at 175 °C for 30 min, followed by an isotopic switch to 1% $^{13}CO$/He for 10 min. Figure 3A (upper graph) shows the IR bands of adsorbed

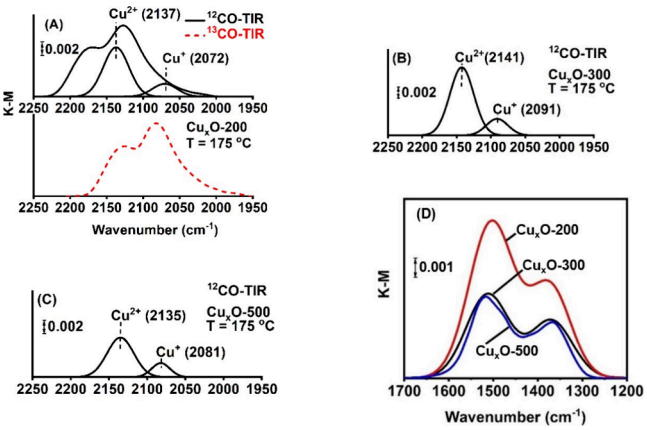


**Figure 3.** (A) *In situ* DRIFTS spectra recorded in the 2250−1950 $cm^{-1}$ range after 30 min in $^{12}CO$/He at 175 °C (upper graph) followed by the gas switch 1 vol % $^{12}CO$/He (30 min) → 1 vol % $^{13}CO$/He (10 min) (lower graph) on the $Cu_xO$-200 catalyst; IR bands of adsorbed CO on $Cu^{2+}$ and $Cu^+$ sites obtained in the 2250−1950 $cm^{-1}$ range after 30 min in $^{12}CO$/He at 175 °C on $Cu_xO$-300 (B) and $Cu_xO$-500 (C) catalysts after deconvolution; (D) *in situ* DRIFTS spectra recorded in the 1700−1200 $cm^{-1}$ range after 30 min in $^{12}CO$/He at 175 °C on the three $Cu_xO$-*T* catalysts.

CO on $Cu^{2+}$ (2137 $cm^{-1}$) and $Cu^+$ (2072 $cm^{-1}$) sites[4,42−45] obtained following deconvolution of the DRIFTS spectrum (2250−1950 $cm^{-1}$) recorded on $Cu_xO$-200 as presented and discussed in Section 3 of the SI (Figure S4 and Figure S5A). Similar deconvolution procedures were performed for the $Cu_xO$-300 (Figure 3B) and $Cu_xO$-500 samples (Figure 3C), and these are depicted in Figure S5B and S5C. Infrared bands appeared at 2141/2091 $cm^{-1}$ and 2135/2081 $cm^{-1}$, respectively, for the $Cu_xO$-300 and $Cu_xO$-500 solids. It is seen that the binding strength of CO adsorbed on $Cu^{2+}$ is lower in the case of $Cu_xO$-300 compared to $Cu_xO$-200 and $Cu_xO$-500 solids, a larger blue shift compared to the Q-branch (Figure S5A−C). Similarly, the binding strength of CO adsorbed on $Cu^+$ is lower in the case of $Cu_xO$-300 compared to $Cu_xO$-200 and $Cu_xO$-500, a smaller red shift compared to the Q-branch. It is important at this point to note that the ratio of the surface concentration of CO-s adsorbed on $Cu^{2+}$ sites to that on $Cu^+$ sites in the three solids does not follow the nominal surface concentration ratio obtained from the XPS analyses (Table 1). This implies that different fractions of exposed $Cu^{2+}$ and $Cu^+$ sites chemisorb CO at 175 °C, and this relates also to the different binding stength of adsorbed CO on the $Cu^{2+}$ and $Cu^+$ sites. This conclusion is supported by the SSITKA study (Section 3.4), where the concentrations of active adsorbed CO-s participating in the CO oxidation reaction at 175 °C (1% CO/20% $O_2$/He) were only 16, 3.4, and 2.4% of the total exposed $Cu^+$ and $Cu^{2+}$.

Following the 1 vol % $^{12}CO$/He gas treatment at 175 °C/30 min, the catalysts were then exposed to the equivalent 1 vol % $^{13}CO$/He isotopic gas mixture for 10 min. In all three solids, the shapes of the $^{13}CO$-IR spectra remained very similar to those observed using the 1 vol % $^{12}CO$/He gas, as well as the ratio of the surface concentration of the two linear CO-s (Figure 3A, and Figure S5A−C). It is important to note that the DRIFTS spectra recorded 15 s after the $^{13}CO$/He isotopic gas switch were very similar to those recorded after 10 min in $^{13}CO$/He. This result implies very fast and reversible CO chemisorption on the three $Cu_xO$-*T* catalytic surfaces. According to the $t_M$ values of the dynamic rate response curves of lattice oxygen reduction by CO appeared between 10 and 26 s (Figure 2A, C/upper graph, Table 2), CO chemisorption cannot be the rate-determining step (RDS) of the reduction of lattice oxygen by CO toward the formation of $CO_2$.

Figure 3D shows the DRIFTS spectra recorded in the 1700−1200 $cm^{-1}$ range after 15 min in 1 vol % CO/He gas treatment at 175 °C. The recorded IR bands highlight the presence of various carbonate-type species, including the monodentate and bidentate/polydentate carbonates. The presence of these species reflects the interactions not only between CO and surface oxygen species on $Cu_xO$-*T* but also between the $CO_2$ gas product and the Cu cations.[42,46−48] These interactions are strongly influenced by the Cu oxidation state, $Cu_xO$ morphology, and extent of oxygen vacant sites present.[47,48] Very similar in shape and position DRIFTS spectra were recorded for all three solids, strongly implying that similar structures of adsorbed carbonate-type species are formed. In the case of the $Cu^+$-rich sample ($Cu_xO$-200), significantly larger concentrations of adsorbed carbonate-type species were noticed, not due to differences in the BET area (max about 30%) but very likely to an enhanced surface concentration of copper sites at the $Cu_2O$-CuO hetero-junctions as previously discussed. The increase of the binding strength of carbonate-type species in the $Cu_xO$-200 compared to the other two samples must be excluded, since thermal stability studies that follow do not support this possibility. In the IR work of Zhang et al.,[48] strong IR bands at 1554 and 1346 $cm^{-1}$ were reported after CO chemisorption at RT over a CuO sample annealed at 527 °C in vacuum. The latter process was used to create $Cu^+$ sites after partially reducing CuO by the removal of lattice oxygen. The positions of these IR bands are very similar to those shown in Figure 3D.

The thermal stability of the various adsorbed carbonate-type species was investigated by recording DRIFTS spectra in the 1700−1200 $cm^{-1}$ range following 30 min of exposure of the solids to 1 vol % $CO_2$/He and a 10 min Ar purge at 175 °C (Figure 4A−C). It is important to mention that no IR bands were detected between 1700 and 2250 $cm^{-1}$, indicating that $CO_2$ does not dissociate at 175 °C on the present $Cu_xO$-*T* solid surfaces. The following observations are also offered:

1. The $Cu_xO$-200 sample, which exhibits the largest $Cu^+/Cu^{2+}$ molar ratio, shows significant reduction in the concentration of adsorbed carbonate-type species after


https://doi.org/10.1021/acscatal.5c06757
ACS Catal. 2026, 16, 5499−5519

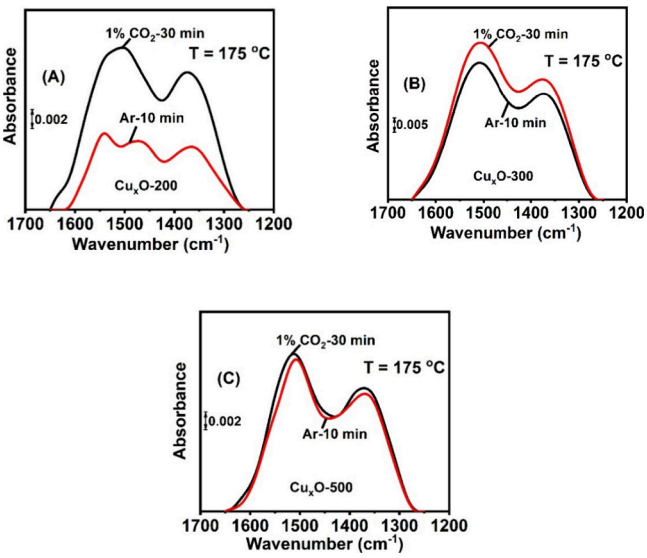


**Figure 4.** DRIFTS spectra recorded in the 1700−1200 $cm^{-1}$ range after 30 min in 1% $CO_2$/He at 175 °C followed by Ar purge (10 min) over (A) $Cu_xO$-200, (B) $Cu_xO$-300, and (C) $Cu_xO$-500 catalysts.

10 min in Ar gas flow (Figure 4A). The IR band at ∼1530 $cm^{-1}$ corresponds to monodentate carbonates ($\nu_{as}$(COO)), while the IR bands in the 1300−1400 $cm^{-1}$ range are due to bidentate carbonates ($\nu$(C=O) and $\nu_{as}$(COO)).

2. The $Cu_xO$-300 sample (Figure 4B) with a significant decrease in $Cu^+/Cu^{2+}$ molar ratio compared to $Cu_xO$-200 shows enhanced thermal stability toward carbonate-type species. This suggests that surface $Cu^{2+}$−O−$Cu^{2+}$ moieties favor stabilization of carbonates.
3. The $Cu_xO$-500 sample (Figure 4C) with the lowest $Cu^+/Cu^{2+}$ molar ratio (∼0.01) demonstrates exceptional thermal stability for the carbonate-type adsorbed species. The DRIFTS spectra indicate that practically no desorption of $CO_2$ occurs after 10 min of Ar purge. It should be noted that $Cu_xO$-300 and $Cu_xO$-500 samples present different primary crystal sizes for CuO as previously reported, which might play a role for the strengthening of bonding between the $CO_2$ and the CuO surface.

The key finding from the *in situ* DRIFTS experiments is the clear correlation between the $Cu^+/Cu^{2+}$ molar ratio and the thermal stability of carbonate-type adsorbed species formed by interactions of CO and $CO_2$ with the $Cu_xO$-*T* surfaces. As the surface $Cu^+/Cu^{2+}$ molar ratio decreases with increasing calcination temperature (Table 1), the thermal stability of the adsorbed carbonate-type species is significantly improved. For the $Cu_xO$-500 sample, having the lowest $Cu^+/Cu^{2+}$ molar ratio of ∼0.01, desorption of $CO_2$ under CO oxidation reaction conditions is expected to be minimal, thus contributing to a larger extent in the poisoning of active lattice oxygen species compared to the other $Cu_xO$-200 and $Cu_xO$-300 solids.

**3.2.4. Redox Cycle (CO Reduction Followed by Reoxidation) in $Cu_xO$-*T* Solids.** Based on the dynamic CO-TIR and $O_2$-TIO kinetic observations (Figure 2), and the *in situ* DRIFTS results regarding the structure and distribution of asorbed CO on $Cu^+$ and $Cu^{2+}$ surface sites (Figure 3), and the adsorbed $CO_2$ thermal stability behavior (Figure 4), the following elementary steps for the redox cycle, namely, reduction of the lattice oxygen ($O_L$) by CO to form $CO_2$(g) and an oxygen vacancy (Vo), followed by the reoxidation of Vo, are proposed:

(i) CO chemisorption step

**Cu (I) sites**

$$Cu^+ - O_L - Cu^+ + CO(g) \leftrightarrow \overset{\overset{\displaystyle CO}{|}}{Cu^+} - O_L - Cu^+ \quad (11)$$

**Cu (II) sites**

$$Cu^{2+} - O_L - Cu^{2+} - O_L + CO(g) \leftrightarrow \overset{\overset{\displaystyle CO}{|}}{Cu^{2+}} - O_L - Cu^{2+} - O_L \quad (12)$$

(ii) Reduction step

$$\overset{\overset{\displaystyle CO}{|}}{Cu^+} - O_L^{2-} - Cu^+ \rightarrow Cu^o - O_V - Cu^o + CO_2(g) \quad (13)$$

$$\overset{\overset{\displaystyle CO}{|}}{Cu^{2+}} - O_L - Cu^{2+} - O_L \rightarrow Cu^+ - O_V - Cu^+ - O_L + CO_2(g) \quad (14)$$

$$\underset{CuO}{[Cu^+ - O_V - \overset{\overset{\displaystyle CO}{|}}{Cu^+}]} + \underset{Cu_2O}{[Cu^+ - O_L - Cu^+]} \rightarrow 2[Cu^+ - O_V - Cu^+] + CO_2(g) \quad (15)$$

(iii) Formation of a carbonate-type chemisorbed $CO_2$ intermediate

Reduction steps in 13−15 consider that an intermediate type of adsorbed $CO_2$-s is bonded very weakly on the reduced $Cu_xO$-*T* surface, and because of this, its surface coverage is practically zero. However, as evidenced from the CO-TIR-DRIFTS (Figure 3D) and $CO_2$ chemisorption-DRIFTS experiments followed by Ar gas treatment (Figure 4A−C), this might not necessarily apply. As the $Cu^+/Cu^{2+}$ ratio decreases, the rate of desorption of $CO_2$-s from the $Cu_xO$-*T* surface is significantly reduced. The following elementary step (reaction 16) exemplifies the formation of $CO_2$-s during CO oxidation by the lattice oxygen of $Cu_2O$ ($Cu^+$).

$$\overset{\overset{\displaystyle CO}{|}}{Cu^+} - O_L^{2-} - Cu^+ - O_L \rightarrow Cu^+ - \underset{\underset{\displaystyle O}{\diagdown}}{\overset{\overset{\displaystyle C}{\diagup}}{O}} - Cu^+ - O_L \quad (16)$$

(iv) Reoxidaton step

$$2[Cu^+ - O_V/2e^- - Cu^+] + O_2(g) \rightarrow 2[Cu^+ - O_L - Cu^+] \quad (17)$$

$$Cu^+ - O_V - Cu^+ - O_L + {}^1\!/_2 O_2(g) \rightarrow Cu^{2+} - O_L - Cu^{2+} - O_L \quad (18)$$

Elementary steps (11) and (12) describe the reversible and fast chemisorption step of CO on $Cu^+$ and $Cu^{2+}$ adsorption sites as evidenced by the dynamic rates of CO conversion upon the step-gas switch He → 1% CO/He (Figure 2A, C/upper graph) and the *in situ* DRIFTS $^{12}CO/^{13}CO$ isotopic exchange experiment (Figure 3A−C). In all three $Cu_xO$-*T* solids, as shown by the XPS results (Figure 2B−C and Table 1), both $Cu^+$ and $Cu^{2+}$ oxidation states exist when the calcination temperature of the c-$Cu_2O$ solid increased from 200 to 500 °C. However, a large drop in the surface at. % concentration of $Cu^+$ was evident when the calcination T increased from 200 to 300 °C (ca. from ∼83 to ∼2.5%). CO chemisorption described by the elementary steps (11) and (12) involve $Cu^+$ and $Cu^{2+}$


https://doi.org/10.1021/acscatal.5c06757
ACS Catal. 2026, 16, 5499−5519

sites and not surface lattice oxygen since the latter requires an activation barrier of 0.4 eV as opposed to the case of copper sites where no barrier is required.[13]

Elementary steps (13−15) describe the reduction of $Cu_xO$-*T* by CO, where chemisorbed CO-s reacts with adjacent lattice oxygen ($O_L$) to form $CO_2$ and an oxygen vacant site ($V_O$). More precisely, adsorbed CO-s formed on the $Cu^+$ sites of reduced CuO reacts with the adjacent surface lattice oxygen ($O_L$) of the $Cu_2O$ phase (heterojunction site). The latter phase provides more labile oxygen, as revealed by the quantitative results reported in Table 2. Elementary step (16) describes the formation of a likely adsorbed structure of carbon dioxide (bridged carbonate)[47] before desorbing from the solid surface. As evidenced by the DRIFTS-$CO_2$ chemisorption and desorption in Ar gas flow experiments (Figure 4A−C), as the $Cu^+/Cu^{2+}$ molar ratio increases, the binding strength of chemisorbed $CO_2$-s becomes weak (compare Figure 4A and C). This important result may suggest that $Cu_xO$-500 with the lowest $Cu^+/Cu^{2+}$ molar ratio is prone to provide a lower CO oxidation rate at 175 °C due to the lowering of available O−Cu−CO sites by the blockage of adsorbed $CO_2$-s. This is supported by the quantitative results presented in Table 2. As the temperature in the CO/He gas treatment increased to 190 °C, the amount of $O_L$ reduced by CO in the $Cu_xO$-500 sample with the largest amount of $Cu^{2+}$ increased significantly, as opposed to the other two samples, where a small decrease was only observed (Table 2). Finally, elementary steps (17) and (18) describe the reoxidation process of reduced $Cu_2O$ and CuO, respectively, during the $O_2$-TIO experiment (Figure 2B, C/lower graph, and Table 2).

The RDS of the redox reaction path described by steps (11−18) is suggested to be the abstraction of $O_L$ by CO-s (reduction step) since reoxidation of surface $V_O$ by gaseous oxygen is a fast step.[21] At the switch to the $O_2$/He (isothermal oxidation step), molecular $O_2$ dissociates on two adjacent surface oxygen vacant sites formed under the CO/He gas treatment (steps (17) and (18)). Other possibilities with favorable energetics for the formation of $O_2$-ads and adsorbed atomic oxygen O-ads on the defective surfaces of CuO(111) and $Cu_2O$(111) were discussed via DFT computations.[21,49−51]

### 3.3. CO Oxidation - Steady State Kinetic Rate Measurements

The effect of the surface concentration of oxidized copper species ($Cu^+/Cu^{2+}$ molar ratio) in the $Cu_xO$-*T* solids on the apparent activation energy ($E_a$, kJ mol$^{-1}$) of the CO oxidation under steady-state reaction conditions is presented in Figure 5. The $E_a$ parameter was estimated at the temperature ranges of 100−150 °C, 160−190 °C, and 170−200 °C, respectively, for the $Cu_xO$-200, $Cu_xO$-300, and $Cu_xO$-500 catalysts, and the following order was found: $E_a$ ($Cu_2O$-200) < $E_a$ ($Cu_2O$-300) < $E_a$ ($Cu_2O$-500). Specifically, the $Cu_xO$-200 catalyst with a $Cu^+/Cu^{2+}$ ratio of ∼5 (Table 2) exhibited the lowest $E_a$ value (80 ± 3.8 kJ/mol), whereas the $Cu_xO$-500 solid with a $Cu^+/Cu^{2+}$ ratio of ∼0.01 exhibited the highest $E_a$ value (125 ± 6.8 kJ/mol). The $Cu_xO$-300 solid with a $Cu^+/Cu^{2+}$ ratio of ∼0.025 exhibited an intermediate value of 103 ± 5.1 kJ/mol. As evidenced by the HRTEM studies (Figure 1D), it is important to recall that oxidation of $Cu_2O$ (cuboctahedron) at 200 °C/1 h ($Cu_xO$-200) follows the Nano Kirkendall Effect (NKE) as previously discussed, resulting in a hollow nanostructure. As previously discussed, an increased concentration of O−$Cu^+$−O−$Cu^{2+}$−O heterojunctions of likely different local chemical environment (recall the likely presence of amorphous CuO on top of c-$Cu_2O$ NCs present in the $Cu_xO$-200 sample) might have been formed, as opposed to the case of $Cu_xO$-300 and $Cu_xO$-500 solids. The increase of primary crystal size of CuO in $C_xO$-500 compared to $Cu_xO$-300 might also be considered to have influenced the energetics of CO oxidation (facet dependence) as reported by Zhang et al.[22] The authors have illustrated via HRTEM, kinetic studies, and DFT computations that the dominant surface sites contributing to the catalytic activity switch from the facet sites for large unsupported c-$Cu_2O$ particles (ca. 445−1030 nm in size) to the edge sites for small c-$Cu_2O$ (34−110 nm in size). This result should be also considered in explaining the catalytic activity results of the present work, where the $Cu_xO$-200 sample consists of smaller $Cu_2O$ (core)-CuO particles compared to the $Cu_xO$-500 solid. The density of the sites in local core/shell-patch architectures on the external surface of the hollow structure of $Cu_xO$-200 (Figure 1D, b), along with that of heterojunctions also present inside the hollow structure (Nano Kirkendall Effect), and the quality of each type of site (site activity) are two important kinetic parameters that explain the large difference in the catalytic activity between high ($Cu_xO$-200) and low ($Cu_xO$-500) $Cu^+$-containing solids.

Pillai and Deevi[17] examined commercial Cu, CuO, and $Cu_2O$ along with synthesized CuO catalysts for their activity toward the CO oxidation reaction. The estimated apparent activation energies were in the range of 88.6−123 kJ mol$^{-1}$ (*T* = 90−140 °C, feed composition: 3.6% CO/21% $O_2$/Ar). Shi et al.[19] conducted a comprehensive investigation of the effect of the $Cu^+/Cu^{2+}$ molar ratio in the $Cu_2O$-CuO heterojunction system (after calcining the pristine $Cu_2O$ in an air atmosphere) on the CO oxidation catalytic activity. The authors concluded that $Cu_2O$-CuO heterostructures as evidenced by Raman, UV−vis, and FTIR spectroscopies presented significantly lower activation energies than $Cu_2O$ ($Cu^+$) and CuO ($Cu^{2+}$) catalysts, the latter exhibiting an $E_a$ value of 165 kJ mol$^{-1}$ compared to 79.0 and 115.8 kJ mol$^{-1}$ obtained for $Cu_2O$-CuO heterostructures with surface $Cu^+/Cu^{2+}$ molar ratios of 0.64 and 0.45, respectively (1% CO/20% $O_2/N_2$, *T* = 80−210 °C). Furthermore, the authors showed that the $Cu_2O$-CuO heterostructures presented increased concentrations of oxygen vacant sites and labile lattice oxygen species. These results are in harmony with those presented in this work regarding oxygen reducibility and $E_a$ for the CO oxidation reaction under similar experimental conditions (Figure 2A−D, Table 2, and Figure 5).

In the following section, advanced transient isotopic experiments (SSITKA technique) linked to the use of mass spectrometry are presented and discussed, aiming to provide mechanistic insights for the catalytic CO oxidation at 175 °C

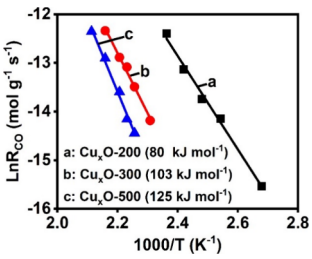


**Figure 5.** Arrhenius plots of the CO conversion rate over the three $Cu_xO$-*T* catalysts.


https://doi.org/10.1021/acscatal.5c06757
ACS Catal. 2026, 16, 5499−5519

under $O_2$-rich conditions (1 vol % CO/20 vol % $O_2$/He). Using only transient isotopic response curves and material balances, we were able to distinguish competing CO oxidation mechanisms on unsupported $Cu_2O$-CuO solids of varying $Cu^+/Cu^{2+}$ molar ratios for the first time.

### 3.4. Mechanistic Studies

**3.4.1. Langmuir–Hinshelwood (L-H) and Mars–van Krevelen (M-vK) Mechanisms.** There has been no work published until now that examines rival CO oxidation mechanisms on real powder $Cu_2O$-CuO heterojunction systems with the structure complexity presented and discussed previously (Figure 1A–D) based only on experimental rate data. There are only a few DFT computations carried out on $Cu_2O(100)$ with a CuO overlayer in an optimized structural form,[22] on CuO and $Cu_2O$ single ideal or defected facets, e.g., $Cu_2O(111)$),[49,52,23] and on CuO(111)-$Cu_2O(110)$ heterojunctions.[21] In the present work, the SSITKA technique coupled with mass spectrometry and DRIFTS was applied on unsupported and polycrystalline $Cu_2O$-CuO solid surfaces to discriminate the most probable among the three most acceptable reaction mechanisms (M-vK, L-H, and E-R mechanisms)[6] for the CO oxidation on $Cu_xO$ surfaces.

The Langmuir–Hinshelwood (L-H) and Mars–van Krevelen (M-vK) mechanisms are largely proposed to operate for the CO catalytic oxidation over metal oxides.[6] In the case of the L-H mechanism and for $Cu_2O$ and CuO single crystal surfaces, CO(g) adsorbs onto $Cu^+$ and $Cu^{2+}$ cationic sites as previously presented and discussed, while $O_2$(g) adsorbs mainly on oxygen vacant sites ($V_O$) to form the $O_2^-$ ($O_2$-ads) species. The latter can further dissociate into two singly adsorbed oxygen species (O-ads).[6,21,22,51] Surface adsorbed intermediates OOCO-s and COO-s can then be formed, leading eventually to $CO_2$(g), with the ability for readsorption on active, but also inactive, surface sites. Conversely, the redox mechanism initially introduced by Mars and van Krevelen (M-vK mechanism) describes a surface reaction wherein the lattice oxygen ($O_{Ls}$) of the metal oxide interacts with adsorbed CO-s, resulting in the formation of a COO-s intermediate and the generation of an oxygen vacancy ($V_O$) on the surface. The COO-s eventually decomposes into $CO_2$(g). The $O_2$(g) then restores the reduced copper oxide surface to its oxidized state.[6] The above information for the mechanism of the CO oxidation reaction is mainly based on DFT computations over ideal and defected $Cu_2O(111)$ and CuO(111) surfaces.

Following the series of pools formalism of SSITKA analysis[32] to describe the carbon pathway in the CO oxidation reaction, Scheme 1 is provided to aid understanding. This scheme aligns with both the Mars–van Krevelen (M-vK) and Langmuir–Hinshelwood (L-H) reaction mechanisms. The additionally proposed Eley–Rideal (E-R) mechanism is analyzed in Section 3.4.2.

**Scheme 1. Carbon Path from CO(g) to $CO_2$(g) in the SSITKA Formalism of a Series of Pools from Reactants to Adsorbed Active Reaction Intermediates to the $CO_2$(g) Product for the CO Oxidation Reaction on Unsupported $Cu_xO$-*T* Catalytic Surfaces**[a]

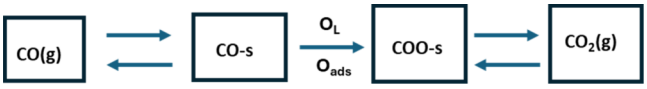


[a]This applies for the M-vK and L-H reaction mechanisms.

Figure 6A presents the response curves of the dimensionless concentration (*Z*) of Kr (tracer gas), $^{13}CO$, and $^{13}CO_2$ at the

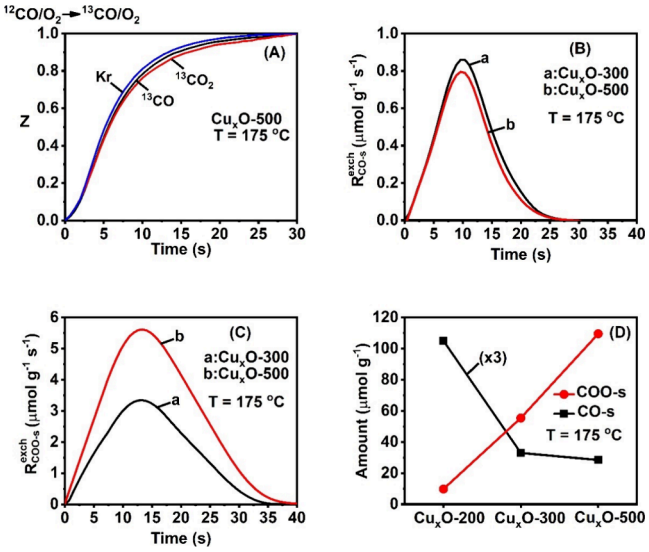


**Figure 6.** (A) Dimensionless concentration (*Z*) dynamic response curves of Kr (tracer), $^{13}CO$(g), and $^{13}CO_2$(g) obtained after the SSITKA switch 1% CO/20% $O_2$/He (30 min) → 1% $^{13}CO$/20% $O_2$/1% Kr/He (*t*) at 175 °C over the $Cu_xO$-500 catalyst; comparison of dynamic $R^{exch}_{CO-s}$ (B) and $R^{exch}_{COO-s}$ (C) exchange rates on $Cu_xO$-300 and $Cu_xO$-500 catalytic materials; (D) concentration (μmol $g^{-1}$) of CO-s and COO-s intermediates formed under steady-state CO oxidation reaction conditions at 175 °C as a function of $Cu^+/Cu^{2+}$ molar ratio in the $Cu_xO$-*T* solids.

SSITKA switch for the $Cu_xO$-500 ($Cu^+/Cu^{2+}$ = 0.01) catalyst sample. The steady-state rate of CO oxidation reaction using $^{12}CO/O_2$/He under the kinetic regime ($X_{CO}$ < 10%), and in the absence of external (within the catalytic bed) and internal (within catalyst particles) mass transport effects, implies constant surface concentrations (or coverages) of $^{12}$CO-s and $^{12}$COO-s and similar concentrations of gaseous CO and $CO_2$ along the catalyst bed in the CSTR microreactor used. At the SSITKA switch to the equivalent $^{13}$**CO**/$O_2$/He gas mixture, $^{12}CO$(g) is quickly replaced by $^{13}CO$(g), and gradually $^{12}$CO-s and $^{12}$COO-s are depleted and replaced by $^{13}$CO-s and $^{13}$COO-s, respectively. As a result of this, the $^{12}CO_2$(g) formation rate will start to decrease (not shown) and that of $^{13}CO_2$ formation to increase toward the same $^{12}CO_2$ concentration value obtained before the SSITKA switch. This dynamic rate of replacement of $^{12}$C-labeled adsorbed species by their corresponding $^{13}$C-labeled ones is governed by the kinetics of the involved elementary reaction steps, which can be described in terms of surface concentrations (or coverages, $\theta$) and rate constants (*k*'s) of associated elementary reaction steps. Based on Scheme 1, the slowest step (rate-determining step, RDS) will largely dictate the SSITKA dynamic response to $^{13}CO_2$(g) formation.

The sequence of the appearance of $^{13}CO$ and $^{13}CO_2$ for $Cu_xO$-500 (Figure 6A) is consistent with Scheme 1, where $^{13}$C (via $^{13}CO$(g)) must pass first through the CO-s pool followed by the pool associated with the COO-s reaction intermediate. Thus, the $^{13}CO_2$(g) dynamic response should lag behind that of $^{13}CO$(g). Very similar SSITKA responses were recorded for the $Cu_xO$-300 catalyst.


https://doi.org/10.1021/acscatal.5c06757
ACS Catal. 2026, 16, 5499–5519

The dynamic rates of CO-s and COO-s exchange, $R^{exch}_{CO\text{-}s}$ and $R^{exch}_{COO\text{-}s}$, respectively, for the CO oxidation reaction have been estimated via appropriate material balances for the first time, and these are described in detail in the Supporting Information (Section 1). Below, we introduce the dynamic exchange rate expressions given by eqs 19 and 20 based on Scheme 1:

$$R^{exch}_{CO-s} = \frac{F_T}{W} y^f_{CO}[Z_{Kr}(t) - (1 - X_{CO})Z_{CO}(t) - 2X_{CO}Z_{CO_2}(t)] \quad (19)$$

$$R^{exch}_{COO-s} = \frac{F_T}{W} y^f_{CO} X_{CO}[Z_{CO}(t) - Z_{CO_2}(t)] \quad (20)$$

The dynamic rates of CO-s and COO-s exchange for the $Cu_xO$-300 and $Cu_xO$-500 catalysts are compared in Figure 6B and C, respectively. Very similar and fast exchange rates for CO-s are observed in both catalytic surfaces, implying very similar concentrations ($\mu$mol $g^{-1}$) of CO-s (after integration of $R^{exch}_{CO\text{-}s}$). On the other hand, significantly larger dynamic rates are observed for the exchange of the COO-s intermediate in the case of $Cu_xO$-500 compared to the $Cu_xO$-300 catalytic surface. Considering the very similar shape of the dynamic rates of $R_{COO\text{-}s}$ exchange (Figure 6C), the higher dynamic rates exhibited by $Cu_xO$-500 is likely due to the higher concentration of active COO-s species formed on the latter catalytic surface compared to that on $Cu_xO$-300. The latter is supported also by the fact that COO-s species formed under 1% CO/20% $O_2$/He were found to be more stable in an $O_2$/He gas atmosphere at 175 °C according to related *in situ* DRIFTS experiments to be described later. It should be noted here that the small difference in the BET area between the $Cu_xO$-300 and $Cu_xO$-500 solids cannot explain the differences in the observed dynamic rates (Figure 6C).

The surface concentration ($\mu$mol $g^{-1}$) of CO-s (eq 4), and thus of the equivalent concentration of $Cu^+$ and $Cu^{2+}$ CO adsorption sites participating in the reaction path, and that of the active COO-s intermediates (eq 5 or 6) established in the carbon path of the CO oxidation reaction as a function of $Cu^+$/$Cu^{2+}$ molar ratio are depicted in Figure 6D. It is shown that the $Cu_xO$-300 and $Cu_xO$-500 solids exhibit practically very similar concentrations of CO-s (~10 $\mu$mol $g^{-1}$), in harmony with the results shown in Figure 6B. On the other hand, the concentrations of active intermediates COO-s (Scheme 1) and/or OCOO-s (eq 16) significantly increase after the $Cu^+$/$Cu^{2+}$ ratio decreases from 0.025 to 0.01 (52 vs 110 $\mu$mol $g^{-1}$ or 4.0 vs 6.9 $\mu$mol $m^{-2}$). Considering surface densities of 11.2 $Cu^+$ atoms/$nm^2$ and 15.5 $Cu^{2+}$ atoms/$nm^2$ for the $Cu_2O(111)$ and CuO(111) facets, respectively, the measured BET areas, the surface copper composition of the three $Cu_xO$-*T* solids (Table 1), and the adsorption stoichiometry of CO-s:Cu ions = 1:1, the concentrations of CO-s in terms of surface coverage, $\theta_{CO}$ (fraction of copper cations covered by CO-s), were estimated to be 0.034 and 0.024, for the $Cu_xO$-300 and $Cu_xO$-500 solids, respectively. This result highlights the fact that only a very small fraction of the surface of unpromoted $Cu_xO$ (polycrystalline form) is covered by CO-s during the CO oxidation reaction (1% CO/20% $O_2$/He; $T$ = 175 °C). In the case of COO-s and OCOO-s active intermediates, values of $\theta$ equal to 0.17 and 0.26, respectively, were estimated for the $Cu_xO$-300 and $Cu_xO$-500 catalytic materials.

The mean residence times of CO-s, $\tau_{CO}$ (s), were estimated to be 0.7 and 0.6 s (eq 7) for the $Cu_xO$-300 and $Cu_xO$-500 catalysts, respectively. The mean residence times of adsorbed carboxylate-type COO-s species, $\tau_{CO2}$ (eq 8, Scheme 1), were estimated to be 0.36 and 1.6 s for the $Cu_xO$-300 and $Cu_xO$-500 catalysts, respectively. This observation corresponds with the activity sequence of these two catalysts, as the rate-determining step (RDS) for both M-vK and L-H mechanisms involves the surface reaction between CO-s and either adsorbed oxygen ($O_{ad}$) or surface lattice oxygen ($O_L$).[6] It is important to note that when an active intermediate has a larger average residence time, it may be considered less reactive.

A comparison between the reactivity of surface lattice oxygen ($O_{Ls}$) and adsorbed oxygen species ($O_{ad}$) toward CO can be attempted based on the dynamic rate results shown in Figure 2A (step-gas switch He → 1% CO/He) and the steady-state (1% CO/20% $O_2$/He) kinetic rate data (Figure 5). As previously discussed, the maximum value in the dynamic rate of CO conversion observed at the initial state of the transient ($R_o$ ($\mu$mol $g^{-1}$ $s^{-1}$), Table 2) truly reflects the interaction of CO(g) with the surface lattice oxygen, $O_{Ls}$. During this very short period, CO consumption was minimal, so its concentration remained close to 1 vol % (feed level). At 175 °C, the $Cu_xO$-200 catalyst shows a $R_o$ value 5.2 times higher than that of $Cu_xO$-500 (Table 2). In the case of the kinetic CO oxidation reaction rate ($R_{CO}$) at 175 °C (CO-conversion less than 12%), the $Cu_xO$-200 sample presents ~13 times larger $R_{CO}$ than the $Cu_xO$-500 one. It is very interesting to compare the ratio of $R_o/R_{CO}$ for the $Cu_xO$-200 and $Cu_xO$-500 solids. It was found that this ratio has values of 0.8 and 1.95 for the $Cu_xO$-200 and $Cu_xO$-500 solids, respectively; a value of 1.2 was estimated for the $Cu_xO$-300 catalytic system.

The above analysis of kinetic initial rate data for the CO oxidation by lattice oxygen (1% CO/He reaction) and under 1% CO/20% $O_2$/He steady-state reaction conditions may reasonably suggest that lattice oxygen appears to prevail compared to an adsorbed oxygen species on the present $Cu_xO$-200 ($Cu^+$ of 83 at. %) and $Cu_xO$-500 ($Cu^+$ of 1 at. %) catalytic systems. Wu et al.[52] reported that on the CuO(111) surface, the activity of an adsorbed atomic oxygen is significantly higher than that of lattice oxygen. This result may not contradict the kinetic analysis presented here, since the reaction rate is strictly dependent on the concentration of adsorbed species. The present work cannot provide information about the relative abundance of $O_{Ls}$ and $O_{ad}$ under CO oxidation reaction conditions.

Based on the above-mentioned comparison between the rates of reduction of lattice oxygen by CO at 175 °C and the kinetic rate of CO oxidation for practically the same $P_{CO}$ and considering that the surface structure under the two experiments was practically similar (use of strongly oxidizing conditions, 20 vol % $O_2$), the M-vK mechanism appears to prevail on the present $Cu_xO$-300 and $Cu_xO$-500 catalytic systems. In the case of $Cu_xO$-200 (large $Cu^+$/$Cu^{2+}$ surface molar ratio), we will showcase next that the prevailing mechanism is that of Eley−Rideal, where the reaction takes place between gaseous CO and the lattice oxygen. The M-vK or L-H mechanism was reported to operate on c-$Cu_2O$-CuO surfaces for large particles (34−110 nm) that mainly expose face sites.[22] The present $Cu_xO$-300 and $Cu_xO$-500 catalysts were found to possess average crystal sizes in this range. Wu et al.[49] have also reported that the M-vK reaction mechanism operates on a defected $Cu_2O(111)$ surface (O/Cu higher than 0.5).


https://doi.org/10.1021/acscatal.5c06757
ACS Catal. 2026, 16, 5499−5519

**3.4.2. Eley–Rideal (E-R) Mechanism.** The Eley–Rideal mechanism involves the direct reaction of CO(g) with surface adsorbed oxygen ($O_{ad}$) or lattice oxygen ($O_L$), leading to the formation of $CO_2$(g).[6] Figure 7 illustrates that the $^{13}$CO(g) response lags that of $^{13}CO_2$(g), as opposed to the case of the $Cu_x$O-500 catalyst (Figure 6A). This experimental result implies that the reaction path as described in Scheme 1 is not the appropriate one for the $Cu_x$O-200 catalyst, where CO-s should not be considered as an active intermediate for the CO oxidation under the stated reaction conditions. The fact that the $^{13}CO_2$(g) transient response curve follows very closely the Kr tracer response (Figure 7) implies also that readsorption of $CO_2$ on the catalyst's surface sites under the present CO oxidation reaction conditions must be excluded or at least be considered very small. DFT computational works on $Cu_2O$ and CuO ideal and defective surfaces support the E-R mechansim.[6,51,23,53]

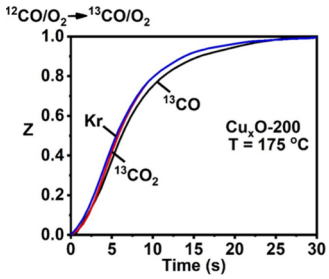


**Figure 7.** Dimensionless concentration ($Z$) dynamic response curves of Kr (tracer), $^{13}$CO(g), and $^{13}CO_2$(g) obtained at the SSITKA switch 1% CO/20% $O_2$/He (30 min) → 1% $^{13}$CO/20% $O_2$/1% Kr/He ($t$) at 175 °C on the $Cu_x$O-200 catalyst.

The significant lag of the response curve of $^{13}$CO(g) relative to that of $^{13}CO_2$(g) (Figure 7) requires an explanation. This behavior can be rationalized by acknowledging that, although the E-R mechanism does not necessitate CO-s, these species may still form as reversibly chemisorbed entities on surface sites unrelated to the CO oxidation pathway. When the SSITKA switch is made from $^{12}CO/O_2$ to $^{13}CO/O_2$, reversibly adsorbed $^{12}$CO-s can be replaced by $^{13}$CO. The estimated amount ($\mu$mol g$^{-1}$) of the involved $^{13}$CO(g) for the exchanged $^{12}$CO-s will show up as additional consumption of $^{13}$CO(g) beyond what is used in the steady state CO oxidation reaction (eq 4). This amount was found to be ∼35 $\mu$mol of CO g$^{-1}$ (Figure 6D, $Cu_x$O-200). In fact, this amount is about three times larger than the active CO-s that participate in the M-vK mechanism for $Cu_x$O-300 and $Cu_x$O-500 catalytic surfaces. Evidence for the reversibility of the CO chemisorption step will be provided below using the SSITKA-DRIFTS technique.

Scheme 2 captures the reaction path via the E-R mechanism over the $Cu_x$O-200 catalytic surface, which possesses the largest concentration of $Cu_2O$-CuO heterojunctions, as previously discussed. According to Scheme 2 and the material balance eq 6, the specific amount of active COO-s intermediates formed in the reaction path was found to be ∼10 $\mu$mol g$^{-1}$, and this is about 11 times lower than that estimated over the $Cu_x$O-500 catalytic surface (Figure 6D). The concentration of CO-s in terms of surface coverage, $\theta_{CO}$ was estimated to be ∼0.16, which is about 6.7 times larger than that found in the case of the $Cu_x$O-500 catalyst. Also, the mean residence time of adsorbed CO-s, $\tau_{CO}$ (s), was estimated to be 2.7 s, larger than that found in the other two catalytic surfaces.

**Scheme 2. Carbon Path from CO(g) to $CO_2$(g) According to the SSITKA Formalism of a Series of Pools from the CO(g) Reactant to Adsorbed Active Reaction Intermediates toward $CO_2$(g) for the CO Oxidation on the Unsupported $Cu_x$O-200 Catalytic System**

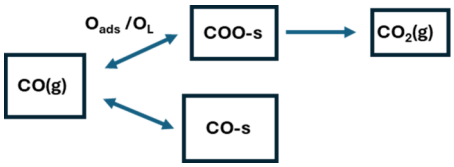


**3.4.3. TOF (s$^{-1}$) Kinetic Rates and Relative Activities ($k_{eff}$) of $Cu_x$O-*T* Catalysts.** The specific kinetic rates of CO oxidation reaction for the $Cu_x$O-$T$ catalysts can be expressed in terms of $TOF_{CO}$ (s$^{-1}$) using the equivalent active sites that accommodate adsorbed CO-s and COO-s intermediates measured by SSITKA (Figure 6D) - working catalytic surface - and the specific steady-state kinetic rates ($\mu$mol g$^{-1}$ s$^{-1}$). It was estimated that the $TOF_{CO}$ values at 175 °C were 1.7 s$^{-1}$, 2.0 × 10$^{-2}$ s$^{-1}$, and 4.5 × 10$^{-3}$ s$^{-1}$ for the $Cu_x$O-200, $Cu_x$O-300, and $Cu_x$O-500 catalysts, respectively. It is thus illustrated that copper sites on the $Cu_x$O-200 surface having a large concentration of $Cu^+$ ($Cu^+/Cu^{2+}$ ∼ 5) are more than 2 orders of magnitude (ca. ∼375 times) more active than those formed on $Cu_x$O-500 ($Cu^+/Cu^{2+}$ ∼ 0.01). This $TOF_{CO}$ site activity parameter is an important quantitative result of this work for the unsupported copper oxide catalytic surfaces reported for the first time. Wei et al.[20] reported activity profiles (CO-conversion vs $T$, 1% CO, $O_2$/CO = 3) for hollow $Cu_2O$-CuO nanospheres of similar size (∼180 nm) and BET area (∼11 m$^2$ g$^{-1}$) with tunable $Cu^{2+}/Cu^+$ ratios (ca. 5.6–8.6) or $Cu^+$ concentrations (ca. 11.6–17.8 at. %). A volcano-type profile of $T_{50}$ (the temperature at which 50% of CO was converted) vs $Cu^{2+}/Cu^+$ ratio was obtained, with a $Cu^{2+}/Cu^+$ of 7.2 (or 86% $Cu^{2+}$) to present the lowest $T_{50}$ (highest activity). In the present work, the existence of a volcano-type TOF (s$^{-1}$) vs $Cu^+/Cu^{2+}$ plot cannot be established since only three tunable ratios are presented. However, it is interesting to note that the highest reaction rate in terms of mol CO g$^{-1}$ s$^{-1}$ or TOF (s$^{-1}$) was obtained using 83 at. % $Cu^+$ in the present $Cu_x$O-200 system compared to the highest specific rate (mol CO g$^{-1}$ s$^{-1}$) obtained with ∼14% $Cu^+$ in the work of Wei et al.[20] It should be mentioned, however, that much less oxidizing conditions were used in that work ($O_2$/CO = 3) compared to the present work ($O_2$/CO = 20). Xu et al.[16] reported on the activity of $Cu_2O$-CuO hollow sphere heterojunction catalytic systems for the CO oxidation reaction (1% CO, $O_2$/CO = 20) in the 80–200 °C range. They found an inverse volcano-type of $T_{50}$ vs $Cu^+/Cu^{2+}$ ratio in the 1.4–1.1 range, where the lowest $T_{50}$ (maximum activity) was obtained for $Cu^+/Cu^{2+}$ = 1.2 compared to the value of ∼5 found in the present work. Across these studies, achieving the optimal $Cu^+/Cu^{2+}$ molar ratio has been linked to improved catalytic performance, primarily due to the increased surface lattice oxygen reducibility in both CuO and $Cu_2O$, as well as a higher concentration of surface oxygen vacancies because of the formation of $Cu_2O$-CuO heterojunctions. Another example that demonstrates the role of the $Cu^+/Cu^{2+}$ molar ratio in Cu-based metal oxides for catalytic oxidation reactions is that of Cu-doped $TiO_2$ (solid solution) used in ethylene oxidation.[54] Once again, a volcano-shaped relationship was observed when plotting TOF (mol $C_2H_4$/mol Cu/s) against Cu (wt %). The


https://doi.org/10.1021/acscatal.5c06757
ACS Catal. 2026, 16, 5499–5519

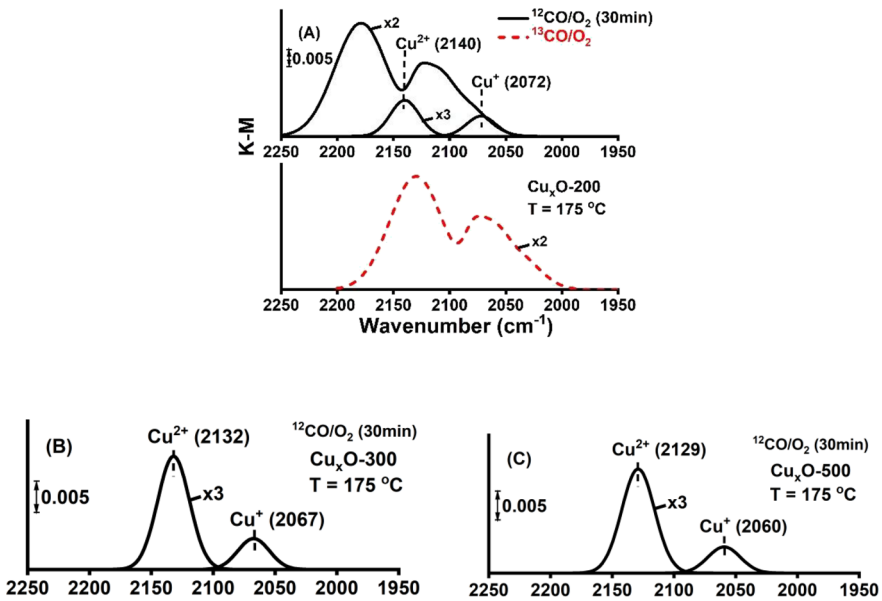


**Figure 8.** (A) IR bands of adsorbed CO on $Cu^{2+}$ and $Cu^{+}$ sites following deconvolution of the DRIFTS spectrum (2250−1950 $cm^{-1}$) recorded after 30 min of 1% $^{12}CO$/20% $O_2$/He gas treatment at 175 °C (upper panel) of $Cu_xO$-200. DRIFTS spectrum recorded after 15 min of the SSITKA switch $^{12}CO/O_2 \rightarrow {}^{13}CO/O_2$ (lower panel); IR bands of adsorbed CO on $Cu^{2+}$ and $Cu^{+}$ sites following deconvolution of the DRIFTS spectrum recorded after 30 min of 1% $^{12}CO$/20% $O_2$/He gas treatment at 175 °C on (B) $Cu_xO$-300 and (C) $Cu_xO$-500 solids.

optimal ratio of surface $Cu^{+}/Cu^{2+}$ in the doped-titania structure was linked to the formation of $V_O$ sites, which are responsible for $O_2$ chemisorption, and the presence of $Cu^{+}/Cu^{2+}$ sites crucial for ethylene adsorption.

For the M-vK mechanism in $Cu_xO$-300 and $Cu_xO$-500 systems (Scheme 1), with the surface reaction between CO-s and mainly lattice oxygen ($O_L$) as the rate-determining step, the oxidation rate of the CO can be approximated as follows:

$$R_{CO}(\mu\text{mol g}^{-1}\text{s}^{-1}) = k_{eff}C_{CO}C_O \quad (21)$$

where $k_{eff}$ is an effective rate constant reflecting the likely contribution to a small extent of the L-H mechanism. $C_{CO}$ and $C_O$ represent the surface concentrations ($\mu$mol $m^{-2}$) of active adsorbed CO-s and lattice oxygen/adsorbed oxygen species, respectively. After using the SSA ($m^2$ $g^{-1}$) of each solid and the $C_{CO}$ and $C_{O\text{-}s}$ concentrations expressed in units of $\mu$mol $g^{-1}$, the relative effective site activity ($k_{eff}$) for the two catalytic systems can be estimated according to the following relationship:

$$k_{eff}{}^{I}/k_{eff}{}^{II} = (R^{I}/R^{II}) \times (C_{CO}{}^{II}C_{O}{}^{II}) \times (SSA^{I}/SSA^{II})^2 \times (C_{CO}{}^{I}C_{O}{}^{I}) \quad (22)$$

In eq 22, "I" stands for $Cu_xO$-300 and "II" for the $Cu_xO$-500 catalytic system. We assume that the $C_O{}^{I}/C_O{}^{II}$ ratio during the $CO/O_2$ reaction in both solids is similar to that obtained from the oxygen titration following the CO/He treatment (Table 2, $O_2$/He switch). After substitution in eq 22 of all the known parameters, it is estimated that $k_{eff}{}^{I} \sim 1.7\ k_{eff}{}^{II}$. This result is in harmony with the lower apparent activation energy of CO oxidation on $Cu_xO$-300 compared to $Cu_xO$-500 according to the independent steady-state kinetic rate measurements reported in Figure 5.

**3.4.4. SSITKA-DRIFTS.** SSITKA-DRIFTS investigations were conducted to elucidate the chemical structure of active intermediates involved in the CO oxidation reaction at 175 °C. Of particular interest was to correlate the distribution of the various adsorbed CO-s species and the presence of active and inactive carbonate-type adsorbed species populated under CO oxidation reaction conditions with the $Cu^{+}/Cu^{2+}$ surface molar ratio. Figure 8A (upper graph) shows the IR bands of adsorbed CO on $Cu^{2+}$ and $Cu^{+}$ sites obtained following deconvolution of the DRIFTS spectrum (2250−1950 $cm^{-1}$) recorded after 30 min in 1% $^{12}CO$/20%$O_2$/He gas treatment at 175 °C for the $Cu_xO$-200 (Figure S6A, SI); Figure 8A (lower graph) is the DRIFTS spectrum recorded after 15 min in $^{13}CO/O_2$/He gas treatment (red-shifted compared to that recorded under $^{12}CO/O_2$/He (upper graph)). It has been reported[55−60] that adsorption of CO on $Cu^{2+}$ generates an IR band in the 2170−2140 $cm^{-1}$ range, while adsorption of CO on $Cu^{+}$ and $Cu^{0}$ forms IR bands in the 2140−2100 and 2100−2000 $cm^{-1}$ ranges, respectively. The gaseous IR band of CO(g) overlaps with that of CO adsorption on $Cu^{2+}$ sites (Figure S6). We will later show that CO does adsorb on $Cu^{2+}$ sites when exposed to 1% CO/20% $O_2$/He at 175 °C. It should be recalled at this point that adsorption of CO on $Cu^{2+}$ sites was also observed under the 1% CO/He gas treatment of $Cu_xO$-*T*, as previously presented and discussed (Figure 3).

The IR bands of the adsorption of CO on the $Cu^{2+}$ and $Cu^{+}$ sites for $Cu_xO$-300 and $Cu_xO$-500 catalysts are depicted in Figure 8B and C, respectively. The IR band due to CO adsorption on $Cu^{2+}$ appeared at 2140, 2132, and 2129 $cm^{-1}$ in the case of $Cu_xO$-200, $Cu_xO$-300, and $Cu_xO$-500 catalysts, respectively, while that on $Cu^{+}$ surface sites at 2072, 2067, and 2060 $cm^{-1}$, respectively. A small but consistent red shift was seen for both CO adsorbed species with decreasing $Cu^{+}/Cu^{2+}$ molar ratio. On the other hand, the integral band intensity ratio of $Cu^{2+}$-CO to $Cu^{+}$-CO was found to increase with increasing $Cu^{2+}$ concentration in the $Cu_2O$-CuO catalytic system. These integral band intensity ratios were found to be 1.8, 3.7, and 4.0 for $Cu^{2+}$ surface at. % concentrations of 17, 97.5, and 99.0% in the $Cu_xO$-*T* samples, respectively (Table 1). This feature is related not only to the relative abundance of $Cu^{2+}$ and $Cu^{+}$ on the surface (first atomic layer) and the


https://doi.org/10.1021/acscatal.5c06757
ACS Catal. 2026, 16, 5499−5519

relative reactivity toward $O_L$ of $Cu^{2+}$-CO and $Cu^{+}$-CO under reaction conditions but also to the relative thermal stability of the two CO adsorbed states.

All three catalytic samples showed the red isotopic shift (ca. 30−35 $cm^{-1}$) in both $Cu^{2+}$-CO and $Cu^{+}$-CO under the $^{13}CO/O_2/He$ gas treatment (Figure 8A and Figure S6, lower graphs). In the case of the $Cu_xO$-200 catalyst, there is a pool of CO-s that does not participate in the formation of $CO_2$ (see Scheme 2) but simply exchanges with $^{13}CO$ (reversible CO chemisorption) as evidenced by the SSITKA-MS results (Figure 7) previously discussed. This is justified by the red shift observed during the SSITKA-DRIFTS experiment (Figure 8A, bottom graph).

Figure S7A−C shows the recorded spectra in the 1650−1250 $cm^{-1}$ IR region after 30 min in 1% CO/20% $O_2$/He at 175 °C before the SSITKA switch. Five vibrational modes were resolved after deconvolution. The IR bands centered at 1569 and 1300−1322 $cm^{-1}$ and which are associated with bidentate carbonates (symmetric and antisymmetric stretching of O−C−O, respectively)[45,56] were consistently observed in all three $Cu_xO$-$T$ solids. The 1510−1514 and 1450−1452 $cm^{-1}$ IR bands are attributed to carboxylates as a result of CO interaction with the Cu−O sites, whereas the IR band at 1368 $cm^{-1}$ is attributed to polydentate carbonates.[33,42,45,46] Based on the integral band areas observed in Figure S7A−C, the distribution of carbonate-type species appears to be influenced by the surface $Cu^{+}/Cu^{2+}$ molar ratio.

After 10 min of $^{13}CO/O_2/He$ (SSITKA switch), very similar DRIFTS spectra to those observed in $^{12}CO/O_2/He$ were recorded without resolving the expected isotopic shift of the O−$^{13}$C−O stretching mode. This result highlights not only the small concentration of active carboxylate (−COO) species present in the reaction path (see Scheme 1) but also the high thermal stability of inactive chemisorbed $CO_2$-s (carbonate-type) species, in agreement with the *in situ* DRIFTS results of $CO_2$ chemisorption followed by Ar purge (Figure 4). The thermal stability of carbonates under $CO/O_2$ reaction conditions was probed, and the results are presented below.

### 3.5. Thermal Stability of Carbonates in an $O_2$/He Gas Atmosphere

The thermal stability of carbonate-type species toward oxygen (20% $O_2$/He), the former produced under 1% CO/20% $O_2$/He reaction (175 °C/30 min), was probed by recording the DRIFTS spectra in the 1700−1200 $cm^{-1}$ region under the $O_2$/He gas flow (Figure 9A−C). For the $Cu_xO$-200 catalyst, the most active solid for the CO oxidation reaction among the series of $Cu_xO$-$T$ materials (Section 3.3), carboxylate and polydentate carbonates completely disappeared within 1 min after the introduction of $O_2$/He, while bidentate carbonates gradually decomposed and disappeared after 90 s in the $O_2$/He gas atmosphere. In the case of $Cu_xO$-300 and $Cu_xO$-500 solids with very low $Cu^{+}/Cu^{2+}$ molar ratios (∼0.025 and 0.01, respectively), the concentrations of carboxylate and other carbonate-type species decreased only slightly after 10 min in 20%$O_2$/He. This result provides evidence that the binding strength of carbonate-type species might play a role in the determination of the CO oxidation activity on $Cu_xO$ solids of varying $Cu^{+}$ and $Cu^{2+}$ surface concentrations. This has also been discussed for various $CuO_x/CeO_2$ low-T CO oxidation catalysts.[57,61]

DRIFTS spectra in the CO-region (2000−2250 $cm^{-1}$) at various times in 20% $O_2$/He gas treatment are provided in

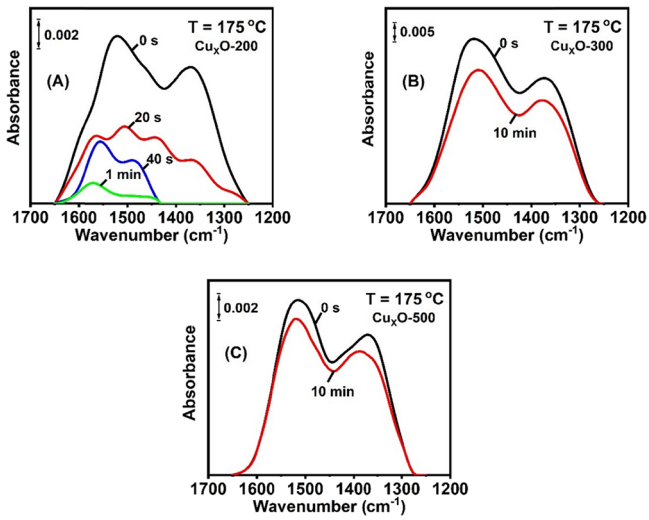


**Figure 9.** *In situ* DRIFTS spectra recorded in the 1700−1200 $cm^{-1}$ range after 30 min in $CO/O_2$ ($t$ = 0 s) at 175 °C, followed by the switch to 20% $O_2$/He ($t$) over (A) $Cu_xO$-200, (B) $Cu_xO$-300, and (C) $Cu_xO$-500 catalysts.

Figure S8. It can be seen that after 40 s in the $O_2$/He gas , only very little adsorbed CO was evident. It should be clarified at this point that the time required to purge completely the 1% CO(g) from the switching valve to the exit of the DRIFTS cell (gas lines and cell volume) was less than 15 s (50 mL/min). Thus, the small surface concentration of CO recorded under this experiment proves that the adsorbed CO on the $Cu^{2+}$ and $Cu^{+}$ sites does exist, and this highlights the correctness of the analysis of the SSITKA-DRIFTS spectra shown in Figure 8A−C and Figure S6A−C.

The remarkable difference observed in the thermal stability of carbonate-type adsorbed species in a 20% $O_2$/He gas atmosphere when the $Cu^{2+}$ surface concentration in the $Cu_2O$-CuO system increases (Figure 9A−C) might be linked to the CO oxidation activity via the apparent activation energy (Figure 5) and TOF ($s^{-1}$) previously discussed. Wang et al.[21] via $CO_2$-TPD characterization of $Cu_2O$-CuO heterojunction catalysts reported a significant drop in the $T_{max}$ value (the temperature at which $CO_2$ desorption rate is maximum) and amount of $CO_2$ desorbed at low temperatures compared with the pristine $Cu_2O$ and CuO metal oxides. This is anticipated to enhance both the number of oxygen adsorption sites and the concentration of oxygen vacancies per surface area in view of the $CO_2$ chemisorption step illustrated in eq 16. Consequently, this is expected to facilitate higher CO oxidation rates at reduced temperatures.

### 3.6. Probing Changes in the Surface $Cu^{+}/Cu^{2+}$ Distribution from Synthesis to CO Oxidation Reaction Conditions

In the present work, *in situ* CO-DRIFTS was used as an alternative methodology (see Section 2.6.1) to the NAP-XPS to investigate the influence of CO oxidation reaction conditions on the distribution of surface Cu oxidation states in the prepared $Cu_2O$-CuO ($Cu_xO$-$T$) catalytic system (see Section 2.1). Figures S9 and S10 report the recorded DRIFTS spectra and the $Cu^{2+}$-CO (2135/2137 $cm^{-1}$) and $Cu^{+}$-CO (2072/2081 $cm^{-1}$) IR bands obtained after deconvolution (see Section 3, SI) for the $Cu_xO$-200 and $Cu_xO$-500 catalytic samples, respectively. The ratio of the integral band area of $Cu^{2+}$-CO to that of $Cu^{+}$-CO was estimated for the case of CO


https://doi.org/10.1021/acscatal.5c06757
ACS Catal. 2026, 16, 5499−5519

adsorption at room T on the fresh catalytic surfaces (Figure S9A and Figure S10A) and that after CO oxidation reaction at 175 °C for 30 min (1% CO/20% $O_2$/He, Figures S9B and S10B). The ratios were found to be 4.55 (fresh sample) and 4.35 (after CO oxidation) for the $Cu_xO$-200 catalytic system (Figure S9) and 4.93 vs 4.63, respectively, for the $Cu_xO$-500 one (Figure S10). These results showcase that the CO oxidation reaction at the specified experimental conditions applied had only a small influence on the distribution of the two surface oxidation states of Cu, namely, 4.3% and 6.1%, respectively, for the $Cu_xO$-200 and $Cu_xO$-500 catalysts. This result highlights also the correct correlations derived in the present work between the surface $Cu^+/Cu^{2+}$ molar ratio (derived from the ex situ XPS analysis of the Cu 2p signal) and the various SSITKA kinetic and redox dynamic parameters of the unsupported $Cu_2O$-CuO catalytic system.

## 4. CONCLUSIONS

This study examines the significant impact of the surface $Cu^+/Cu^{2+}$ molar ratio, as determined by XPS analysis within the 0.01−5.0 range, on both the catalytic CO oxidation activity and the composition of the adsorbed phase for the unsupported $Cu_2O$-CuO heterojunction system. This investigation also explores the influence of the surface $Cu^+/Cu^{2+}$ molar ratio on the mechanism of CO oxidation (1% CO/20% $O_2$/He) at low temperatures. At 175 °C, the catalyst with hollow morphology ($Cu_xO$-200) showed the highest activity, which was associated with its largest $Cu^+/Cu^{2+}$ molar ratio among those tested, and it promoted the Eley−Rideal mechanism, as confirmed by SSITKA-MS analysis. In this case, gaseous CO reacts largely with surface lattice oxygen, part of which is formed on the inherent oxygen vacancies created by the presence of $Cu_2O$-CuO heterojunctions (dynamic oxygen uptake studies). At the same time, linear and reversibly adsorbed CO is formed on the $Cu^+$ and $Cu^{2+}$ sites (SSITKA-DRIFTS), the surface coverage of which was found to be only 0.16 at 175 °C (SSITKA-MS).

The presence of labile and active lattice oxygen toward CO and the formation of oxygen vacancies were probed by dynamic lattice oxygen reduction by CO and reoxidation experiments. In the case of the $Cu_xO$-200 ($Cu^+/Cu^{2+}$ = 4.9) catalyst, at 175−190 °C and after 15 min in CO/He, ∼10 equiv monolayers of lattice oxygen ($N_O$) were reduced, while at 190 °C and after 2 h time on stream, significantly larger amounts were measured.

As the $Cu^+/Cu^{2+}$ molar ratio decreased from 4.9 to 0.01−0.025, where the CuO phase is dominant and the primary crystal size of CuO is in the 32−56 nm range, the CO oxidation follows the M-vK type mechanism (as opposed to the Eley−Rideal mechanism followed by the $Cu_xO$-200 catalyst) for which adsorbed CO-s and O-s species (largely lattice oxygen) participate toward the formation of $CO_2$. The surface coverage of COO-s (carboxylate) active intermediates leading to $CO_2$(g) at 175 °C (SSITKA-MS) was found to double after decreasing the $Cu^+/Cu^{2+}$ molar ratio from 0.025 to 0.01, while very small and similar concentrations for adsorbed CO-s ($\theta_{CO}$ ∼ 0.024−0.034) were found in the two solids. The dynamics of exchange of CO-s and COO-s in the $^{12}CO/O_2 \rightarrow {}^{13}CO/O_2$ SSITKA step-gas switch was analyzed for the first time, highlighting the influence of the $Cu^+/Cu^{2+}$ surface molar ratio on the adsorption/desorption of CO and the reactivity of COO-s intermediates toward the formation of $CO_2$(g).

The specific activity of the $Cu_xO$-*T* solids in terms of $TOF_{CO}$ ($s^{-1}$), which was estimated based on the active sites participating in the CO oxidation at 175 °C (CO-s and COO-s intermediates) followed the order $Cu_xO$-500 < $Cu_xO$-300 < $Cu_xO$-200. The most active $Cu_xO$-200 catalyst containing the largest surface $Cu^+/Cu^{2+}$ molar ratio (ca. 4.9; $d_{avg}$ ($Cu_2O$) ∼ 16 nm) showed an impressively higher $TOF_{CO}$ value by ∼375-times compared to $Cu_xO$-500 of the lowest $Cu^+/Cu^{2+}$ molar ratio (ca. 0.01; $d_{avg}$ (CuO) ∼ 56 nm). These $TOF_{CO}$ ($s^{-1}$) values are reported for the first time for unsupported $Cu_2O$-CuO and CuO catalytic materials. In the case of $Cu_xO$-300 and $Cu_xO$-500 solids, consisting mainly of the CuO phase, while the former has a surface $Cu^+/Cu^{2+}$ ratio about twice as large as the latter case, and a mean primary crystal size of ∼32 nm compared to ∼56 nm, an apparent rate constant ($k_{app}$) for the CO oxidation at 175 °C of 1.7 times larger was estimated.

Time resolved DRIFT spectra for the thermal stability and activity toward oxygen (20% $O_2$/He) of adsorbed CO-s, carboxylate (COO-s), and carbonate-type species formed under CO oxidation at 175 °C/30 min were collected as a function of $Cu^+/Cu^{2+}$ molar ratio. In all cases, similar depletion rates of adsorbed CO-s in 20% $O_2$/He were observed, as opposed to the case of carboxylate- and carbonate-type adsorbed species. Notably, $Cu_xO$-200 of the highest $Cu^+/Cu^{2+}$ molar ratio proved to populate significantly less thermally stable carbonates than the other two solids of very low $Cu^+/Cu^{2+}$ molar ratio (ca. 0.01−0.025). This result aligns with the notably higher $TOF_{CO}$ ($s^{-1}$) observed in $Cu_xO$-200 compared to those of the other catalytic materials ($Cu_xO$-300 and $Cu_xO$-500), indicating that the enhanced activity of this material might be partly attributed to significantly reduced "$CO_2$-poisoning" of surface-active sites during low-temperature CO oxidation.

For the first time, *in situ* CO chemisorption DRIFTS was employed to study how CO oxidation reaction conditions affect the distribution of surface copper oxidation states ($Cu^+/Cu^{2+}$ molar ratio) in the unsupported $Cu_2O$-CuO heterojunction system. This methodology may serve as an alternative to NAP-XPS. Its effective implementation relies on accurate deconvolution of the DRIFTS spectrum within the CO-IR region, where overlapping signals from gaseous CO are present. Conversely, this approach does not encounter the pressure gap obstacle that remains present in the NAP-XPS analysis.

The SSITKA-mass spectrometry technique, along with dynamic isothermal reduction by CO experiments of lattice oxygen of the $Cu_2O$-CuO system, efficiently differentiates the CO oxidation reaction mechanisms, and it is more straightforward and less time-consuming than microkinetic analysis of steady-state rates. On the other hand, mathematical modeling attempts of the SSITKA-MS response curves (involving microkinetic modeling) would provide details of the elementary steps (nature and RDS). Utilizing SSITKA data for modeling, rather than relying solely on steady-state rate measurements, is regarded as a more precise approach. The total surface coverage of the active species determined by SSITKA serves as a valuable constraint, enabling enhanced accuracy in predicting kinetic rate constants of elementary steps.

The future direction of this work might involve applying advanced *operando* NEXAFS to determine the structures of specific surface $Cu^+$ and $Cu^{2+}$ sites, especially at the $Cu_2O$-CuO heterojunctions that are responsible for CO oxidation.[62]


https://doi.org/10.1021/acscatal.5c06757
ACS Catal. 2026, 16, 5499−5519

It is important to note that only a small proportion of $Cu^{+}/Cu^{2+}$ sites is involved in the CO oxidation reaction. Additionally, using NAP-XPS would be highly beneficial to show how variables such as temperature ($T$), partial pressures of CO ($P_{CO}$), $O_2$ ($P_{O2}$), and $CO_2$ ($P_{CO2}$) influence the distribution of $Cu^{+}/Cu^{2+}$ on the surface. When combined with the current SSITKA-MS technique, this approach can help establish valuable relationships between SSITKA kinetic parameters and the surface composition of $Cu^{+}/Cu^{2+}$ as a function of the operational conditions of the reaction.

## ■ ASSOCIATED CONTENT

### Supporting Information

The Supporting Information is available free of charge at https://pubs.acs.org/doi/10.1021/acscatal.5c06757.

$^{13}$C-material balances for $^{13}$CO-SSITKA ($^{12}CO/O_2 \rightarrow {}^{13}CO/O_2$) in terms of dynamic exchange rates of adsorbed CO-s and carboxylate-type active species, Cu LMM Auger peaks, bright-field TEM micrographs and SAED patterns, $N_2$ adsorption−desorption isotherms (77 K) for the $Cu_xO$-$T$ samples, DRIFTS spectra deconvolution analysis, DRIFTS spectra under $^{12}$CO/He and $^{13}$CO/He gas switches, DRIFTS spectra before and after the SSITKA switch for the CO oxidation reaction, DRIFTS spectra under the $O_2$/He gas treatment following CO oxidation at 175 °C over the $Cu_xO$-$T$ catalysts, analysis of DRIFTS spectra of adsorbed CO-s at room T before and after CO oxidation for probing changes in surface $Cu^{+}/Cu^{2+}$ distribution (PDF)

## ■ AUTHOR INFORMATION


### Corresponding Authors

**Sotirios Christodoulou** − *Department of Chemistry, Inorganic Nanocrystals Laboratory, University of Cyprus, 2109 Nicosia, Cyprus;* orcid.org/0000-0001-7020-3661; Email: christodoulou.sotirios@ucy.ac.cy

**Angelos M. Efstathiou** − *Department of Chemistry, Heterogeneous Catalysis Laboratory, University of Cyprus, 2109 Nicosia, Cyprus;* orcid.org/0000-0001-8393-8800; Email: efstath@ucy.ac.cy

### Authors

**Michalis A. Vasiliades** − *Department of Chemistry, Heterogeneous Catalysis Laboratory, University of Cyprus, 2109 Nicosia, Cyprus;* orcid.org/0000-0002-1568-1158

**Georgia-Maria D. Zarkou** − *Department of Chemistry, Heterogeneous Catalysis Laboratory and Department of Chemistry, Inorganic Nanocrystals Laboratory, University of Cyprus, 2109 Nicosia, Cyprus;* orcid.org/0009-0005-5798-6987

**Cheng Zhang** − *Department of Chemistry, Heterogeneous Catalysis Laboratory, University of Cyprus, 2109 Nicosia, Cyprus; College of Chemistry and Environmental Engineering, Shenzhen University, Shenzhen 518060, China*

**Alexandra Theodosiou** − *Department of Chemistry, Inorganic Nanocrystals Laboratory, University of Cyprus, 2109 Nicosia, Cyprus;* orcid.org/0009-0004-6459-1935

**Mirko Prato** − *Materials Characterization Facility, Istituto Italiano di Tecnologia, 16163 Genova, Italy;* orcid.org/0000-0002-2188-8059

**Sašo Gyergyek** − *Department for Materials Synthesis, Jožef Stefan Institute, SI-1000 Ljubljana, Slovenia;* orcid.org/0000-0002-7325-2984

**Petar Djinović** − *Department of Inorganic Chemistry and Technology, National Institute of Chemistry, SI-1000 Ljubljana, Slovenia;* orcid.org/0000-0002-5974-9118

Complete contact information is available at: https://pubs.acs.org/10.1021/acscatal.5c06757


### Author Contributions

[§]M.A.V. and G.-M.D.Z. equally contributed.

### Author Contributions

Conceptualization, A.M.E.; methodology, A.M.E., C.Z., M.A.V., and G.-M.D.Z.; formal analysis, M.A.V., C.Z., G.-M.D.Z., M.P., and A.T.; investigation, M.A.V., C.Z., A.T., P.D., S.G., and G.-M.D.Z.; resources, A.M.E., S.C.; data curation, M.A.V., C.Z., G.-M.D.Z., M.P., and A.T.; writing- original draft preparation, G.-M.D.Z. and M.A.V.; writing-review and editing, A.M.E., M.A.V., and P.D.; visualization, A.M.E., S.C., and M.A.V.; supervision, A.M.E. and M.A.V.; project administration, A.M.E. and S.C.

### Notes

The authors declare no competing financial interest.

## ■ ACKNOWLEDGMENTS

The Research Committee of the University of Cyprus is gratefully acknowledged for financial support of this work. P.D. acknowledges the Slovenian Research and Innovation Agency (ARIS) for funding through grants P1-0418 and N2-0265. Dr. Matjaž Mazaj is acknowledged for help with the powder XRD analysis.

## ■ REFERENCES


(1) Yu, W.; Porosoff, M. D.; Chen, J. G. Review of Pt-Based Bimetallic Catalysis: From Model Surfaces to Supported Catalysts. *Chem. Rev.* **2012**, *112*, 5780−5817.

(2) Royer, S.; Duprez, D. Catalytic Oxidation of Carbon Monoxide over Transition Metal Oxides. *ChemCatChem.* **2011**, *3*, 24−65.

(3) Liu, K.; Wang, A.; Zhang, T. Recent Advances in Preferential Oxidation of CO Reaction over Platinum Group Metal Catalysts. *ACS Catal.* **2012**, *2*, 1165−1178.

(4) Gamarra, D.; Belver, C.; Fernández-García, M.; Martínez-Arias, A. Selective CO Oxidation in Excess $H_2$ over Copper-Ceria Catalysts: Identification of Active Entities/Species. *J. Am. Chem. Soc.* **2007**, *129*, 12064.

(5) Montini, T.; Melchionna, M.; Monai, M.; Fornasiero, P. Fundamentals and Catalytic Applications of $CeO_2$-Based Materials. *Chem. Rev.* **2016**, *116*, 5987−6041.

(6) Fan, Z.; Gao, F.; Zhang, J.; Yi, L.; Luo, N.; Yi, H.; Tang, X. Advances in CO catalytic oxidation on typical metal oxide catalysts: performance, mechanism and optimization. *J. Mater. Chem. A* **2025**, *13*, 26129−26165. (Review paper)

(7) AlKetbi, M.; Polychronopoulou, K.; Abi Jaoude, M.; Vasiliades, M. A.; Sebastian, V.; Hinder, S. J.; Baker, M. A.; Zedan, A. F.; Efstathiou, A. M. Cu-Ce-La-$O_x$ as efficient CO oxidation catalysts: Effect of Cu content. *Appl. Surf. Sci.* **2020**, *505*, No. 144474.

(8) Cam, T. S.; Omarov, S. O.; Chebanenko, M. I.; Sklyarova, A. S.; Nevedomskiy, V. N.; Popkov, V. I. One step closer to the low-temperature CO oxidation over non-noble $CuO/CeO_2$ nanocatalyst: The effect of CuO loading. *J. Environ. Chem. Eng.* **2021**, *9*, No. 105373.

(9) Mosrati, J.; Abdel-Mageed, A. M.; Vuong, T. H.; Grauke, R.; Bartling, S.; Rockstroh, N.; Atia, H.; Armbruster, U.; Wohlrab, S.; Rabeah, J.; Brückner, A. Tiny species with big impact: High activity of

Cu single atoms on $CeO_2$-$TiO_2$ deciphered by operando spectroscopy. *ACS Catal.* **2021**, *11* (17), 10933−10949.
(10) Wang, B.; Zhang, H.; Xu, W.; Li, X.; Wang, W.; Zhang, L.; Li, Y.; Peng, Z.; Yang, F.; Liu, Z. Nature of active sites on Cu-$CeO_2$ catalysts activated by high-temperature thermal aging. *ACS Catal.* **2020**, *10* (21), 12385−12392.
(11) Avgouropoulos, G.; Ioannides, T. Selective CO oxidation over CuO-$CeO_2$ catalysts prepared via the urea−nitrate combustion method. *Appl. Catal. A: Gen.* **2003**, *244*, 155−167.
(12) Abed, H.; Mosrati, J.; Abdel-Mageed, A. M.; Cisneros, S.; Huyen Vuong, T.; Rockstroh, N.; Bartling, S.; Wohlrab, S.; Brückner, A.; Rabeah, J. Preferential CO oxidation on a highly active Cu single atom catalyst supported by Ce−$TiO_x$. *ChemCatChem* **2022**, *14*, No. e202200923.
(13) White, B.; Yin, M.; Hall, A.; Le, D.; Stolbov, S.; Rahman, T.; Turro, N.; O'Brien, S. Complete CO Oxidation over $Cu_2O$ Nanoparticles Supported on Silica Gel. *Nano Lett.* **2006**, *6* (9), 2095−2098.
(14) Wang, X.; Hanson, J. C.; Frenkel, A. I.; Kim, J.-Y.; Rodriguez, J. A. Time-resolved Studies for the Mechanism of Reduction of Copper Oxides with Carbon Monoxide: Complex behavior of Lattice Oxygen and the Formation of Suboxides. *J. Phys. Chem. B* **2004**, *108*, 13667−13673.
(15) Davó-Quiñonero, A.; Bailón-García, E.; López-Rodríguez, S.; Juan-Juan, J.; Lozano-Castelló, D.; García-Melchor, M.; Herrera, F. C.; Pellegrin, E.; Escudero, C.; Bueno-López, A. Insights into the oxygen vacancy filling mechanism in CuO/$CeO_2$ catalysts: A key step toward high selectivity in preferential CO oxidation. *ACS Catal.* **2020**, *10*, 6532−6545.
(16) Xu, L.; Yang, X.; Shi, Y.; Chen, M.; Xue, Y.; Wu, C.; Qiu, J.; Cheng, G.; Wang, N.; Xu, J.; Hu, X. CO oxidation over the $Cu_2O$/CuO hollow sphere heterojunction catalysts with enhanced low-temperature activities. *Int. J. Hydrogen Energy* **2023**, *48*, 24845−24859.
(17) Pillai, R. P.; Deevi, S. Room temperature oxidation of carbon monoxide over copper oxide catalyst. *Appl. Catal. B: Environ.* **2006**, *64*, 146−151.
(18) Huang, T. J.; Tsai, D. H. CO Oxidation Behavior of Copper and Copper Oxides. *Catal. Lett.* **2003**, *87*, 173−178.
(19) Shi, Y.; Xu, L.; Chen, M.; Yang, B.; Cheng, G.; Wu, C.-E.; Miao, Z.; Wang, N.; Hu, X. Fabricating $Cu_2O$-CuO submicron-cubes for efficient catalytic CO oxidation: The significant effect of heterojunction interface. *J. Ind. Eng. Chem.* **2022**, *105*, 324−336.
(20) Wei, B.; Yang, N.; Pang, F.; Ge, J. $Cu_2O$-CuO Hollow Nanospheres as a Heterogeneous Catalyst for Synergetic Oxidation of CO. *J. Phys. Chem. C* **2018**, *122*, 19524−19531.
(21) Wang, Y.; Yun, J.; Zhu, L.; Cao, B.; Gao, J.; Shi, X.; Huang, Y.; Liu, P.; Zhu, G. Mechanistic study of low-temperature CO oxidation over CuO/$Cu_2O$ interfaces with oxygen vacancy modification. *Appl. Surf. Sci.* **2022**, *603*, No. 154469.
(22) Zhang, Z.; Wu, H.; Yu, Z.; Song, R.; Qian, K.; Chen, X.; Tian, J.; Zhang, W.; Huang, W. Site-Resolved $Cu_2O$ Catalysis in the Oxidation of CO. *Angew. Chem., Int. Ed.* **2019**, *58*, 4276−4280.
(23) Sun, B.-Z.; Chen, W.-K.; Xu, Y.-J. Reaction mechanism of CO oxidation on $Cu_2O$(111): A density functional study. *J. Chem. Phys.* **2010**, *133*, No. 154502.
(24) Zhang, Z.; Zhang, J.; Jia, A.-P.; Lu, J.-Q.; Huang, W. Morphology-Dependent CO Reduction Kinetics and Surface Copper Species Evolution of $Cu_2O$ Nanocrystals. *J. Phys. Chem. C* **2020**, *124*, 21568−21576.
(25) Paolella, A.; Brescia, R.; Prato, M.; Povia, M.; Marras, S.; De Trizio, L.; Falqui, A.; Manna, L.; George, C. Colloidal synthesis of cuprite ($Cu_2O$) octahedral nanocrystals and their electrochemical lithiation. *ACS Appl. Mater. Interfaces* **2013**, *5* (7), 2745−2751.
(26) Fairley, N.; Fernandez, V.; Richard-Plouet, M.; Guillot-Deudon, C.; Walton, J.; Smith, E.; Flahaut, D.; Greiner, M.; Biesinger, M.; Tougaard, S.; Morgan, D.; Baltrusaitis, J. Systematic and collaborative approach to problem solving using X-ray photoelectron spectroscopy. *Appl. Surf. Sci. Adv.* **2021**, *5*, No. 100112.
(27) Costa, C. N.; Christou, S. Y.; Georgiou, G.; Efstathiou, A. M. Mathematical modeling of the oxygen storage capacity phenomenon studied by CO pulse transient experiments over Pd/$CeO_2$ catalyst. *J. Catal.* **2003**, *219*, 259−272.
(28) Perego, C. Experimental methods in catalytic kinetics. *Catal. Today* **1999**, *52*, 133−145.
(29) Vasiliades, M. A.; Makri, M. M.; Djinović, P.; Erjavec, B.; Pintar, A.; Efstathiou, A. M. Dry reforming of methane over 5 wt% Ni/$Ce_{1-x}Pr_xO_{2-\delta}$ catalysts: Performance and characterisation of active and inactive carbon by transient isotopic techniques. *Appl. Catal. B: Environ.* **2016**, *197*, 168−183.
(30) Efstathiou, A. M. Elucidation of Mechanistic and Kinetic Aspects of Water-Gas Shift Reaction on Supported Pt and Au Catalysts via Transient Isotopic Techniques. *Catalysis* **2016**, *28*, 175−236. (Review paper)
(31) Ladesma, C.; Yang, J.; Chen, D.; Holmen, A. Recent approaches in mechanistic and kinetic studies of catalytic reactions using SSITKA technique. *ACS Catal.* **2014**, *4*, 4527−4547.
(32) Shannon, S. L.; Goodwin, G. J. Jr. Characterization of Catalytic Surfaces by Isotopic-Transient Kinetics during Steady-State Reaction. *Chem. Rev.* **1995**, *95*, 677−695.
(33) Polychronopoulou, K.; AlKhoori, A. A.; Efstathiou, A. M.; Jaoude, M. A.; Damaskinos, C. M.; Baker, M. A.; Almutawa, A.; Anjum, D. H.; Vasiliades, M. A.; Belabbes, A.; Vega, L. F.; Zedan, A. F.; Hinder, S. J. Design aspects of doped $CeO_2$ for low-temperature catalytic CO oxidation: Transient kinetics and DFT approach. *ACS Appl. Mater. Interfaces* **2021**, *13*, 22391−22415.
(34) Vasiliades, M. A.; Govender, N. S.; Govender, A.; Crous, R.; Moodley, D.; Botha, T.; Efstathiou, A. M. The Effect of $H_2$ Pressure on the Carbon Path of Methanation Reaction on Co/$\gamma$-$Al_2O_3$: Transient Isotopic and *Operando* Methodology Studies. *ACS Catal.* **2022**, *12*, 15110−15129.
(35) Biesinger, M. C. Advanced analysis of copper X-ray photoelectron spectra. *SIA* **2017**, *49*, 1325−1334.
(36) Zedan, A. F.; Mohamed, A. T.; El-Shall, M. S.; AlQaradawi, S. Y.; AlJaber, A. S. Tailoring the reducibility and catalytic activity of CuO nanoparticles for low temperature CO oxidation. *RSC Adv.* 2018, *8*, 19499−19511, and references therein.
(37) Barreca, D.; Gasparotto, A.; Tondello, E. CVD $Cu_2O$ and CuO Nanosystems characterized by XPS. *Surf. Sci. Spectra* **2007**, *14*, 41−51.
(38) Strand, J.; Shluger, A. L. On the Structure of Oxygen Deficient Amorphous Oxide Films. *Adv. Sci.* **2024**, *11*, No. 2306243.
(39) Susman, M. D.; Vaskevich, A.; Rubinstein, I. A General Kinetic-Optical Model for Solid-State Reactions Involving the Nano Kirkendall Effect. The Case of Copper Nanoparticle Oxidation. *J. Phys. Chem. C* **2016**, *120*, 16140−16152.
(40) Chang, C.-J.; Kang, C.-W.; Pundi, A. Effect of Calcination-Induced Oxidation on the Photocatalytic $H_2$ Production Performance of Cubic $Cu_2O$/CuO Composite Photocatalysts. *Catalysts* **2024**, *14*, 926.
(41) Mel'gunov, M. S. Application of the simple Bayesian classifier for the $N_2$ (77 K) adsorption/desorption hysteresis loop recognition. *Adsorption* **2022**, *29* (5−6), 199−208.
(42) Dandekar, A.; Vannice, M. A. Determination of the Dispersion and Surface Oxidation States of Supported Cu Catalysts. *J. Catal.* **1998**, *178*, 621−639.
(43) Busca, G. FT-IR Study of the Surface of Copper Oxide. *J. Mol. Catal.* 1987, *43*, 225−236, and references therein.
(44) Zecchina, A.; Garrone, E.; Guglielminotti, E. In *Catalysts*; Royal Society of Chemistry: London, Vol. *6*, 1983; p. 90.
(45) Zhang, X.-M.; Tian, P.; Tu, W.; Zhang, Z.; Xu, J.; Han, Y.-F. Tuning the Dynamic Interfacial Structure of Copper-Ceria Catalysts by Indium Oxide during CO Oxidation. *ACS Catal.* **2018**, *8* (6), 5261−5275.
(46) Bera, P.; Cámara, A. L.; Hornés, A.; Martínez-Arias, A. Comparative in Situ DRIFTS-MS Study of $^{12}$CO- and $^{13}$ CO-TPR on CuO/CeO $_2$ Catalyst. *J. Phys. Chem. C* **2009**, *113*, 10689−10695.


https://doi.org/10.1021/acscatal.5c06757
ACS Catal. 2026, 16, 5499−5519

(47) Chen, S.; Cao, T.; Gao, Y.; Li, D.; Xiong, F.; Huang, W. Probing Surface Structures of $CeO_2$, $TiO_2$ and $Cu_2O$ Nanocrystals with CO and $CO_2$ Chemisorption. *J. Phys. Chem. C* **2016**, *120*, 21472−21485.
(48) Zhang, Y.; Liu, Y.; Zhao, R.; Lu, B.; Wang, X.; Qiu, H. Direct spectroscopic comparison of CO adsorption over $CuO_x$ prepared in situ. *Catalysts* **2024**, *14*, 578.
(49) Wu, L.-N.; Tian, Z.-Y.; Qin, W. DFT study on CO catalytic oxidation mechanism on the defective $Cu_2O(111)$ surface. *J. Phys. Chem. C* 2018, *122*, 16733−16740, and references therein.
(50) Dey, S.; Chandra Dhal, G. Controlling carbon monoxide emissions from automobile vehicle exhaust using copper oxide catalysts in a catalytic converter. *Materials Today Chemistry* **2020**, *17*, No. 100282.
(51) Ma, B.; Kong, C.; Lv, J.; Zhang, X.; Yang, S.; Yang, T.; Yang, Z. Cu-$Cu_2O$ Heterogeneous Architecture for the Enhanced CO Catalytic Oxidation. *Adv. Mater. Interfaces* **2020**, *7*, No. 1901643.
(52) Wu, L.-N.; Tian, Z.-Y.; El Kasmi, A.; Arshad, M. F.; Qin, W. Mechanistic study of the CO oxidation reaction on the CuO (111) surface during chemical looping combustion. *Proc. Combust. Inst.* **2021**, *38*, 5289−5297.
(53) Lin, L.; Shi, P.; Yao, L.; Xie, K.; Tao, H.; Zhang, Z.; Wang, Y. First-principles study on CO oxidation on CuO(111) surface prefers the Eley-Rideal or Langmuir-Hinshelwood pathway. *Nanotechnology* **2022**, *33* (20), No. 205504.
(54) Rajendran, K.; Sharma, M.; Jaison, A.; Ankitha, M.; Tiwari, A. D.; Vinod, C. P.; Jagadeesan, D. Oxidation of ethylene by Cu/$TiO_2$: reducibility of $Cu^{2+}$ in $TiO_2$ as a possible descriptor of catalytic efficiency. *Catal. Sci. Technol.* **2023**, *13*, 2330−2339.
(55) Ahasan, M. R.; Wang, Y.; Wang, R. In situ DRIFTS and CO-TPD studies of $CeO_2$ and $SiO_2$ supported $CuO_x$ catalysts for CO oxidation. *Mol. Catal.* **2022**, *518*, No. 112085.
(56) Fang, Y.; Chi, X.; Li, L.; Yang, J.; Liu, S.; Lu, X.; Xiao, W.; Wang, L.; Luo, Z.; Yang, W.; Hu, S.; Xiong, J.; Hoang, S.; Deng, H.; Liu, F.; Zhang, L.; Gao, P.; Ding, J.; Guo, Y. Elucidating the nature of the Cu(I) active site in CuO/$TiO_2$ for excellent low-temperature CO oxidation. *ACS Appl. Mater. Interfaces* **2020**, *12*, 7091−7101.
(57) Hornés, A.; Bera, P.; Cámara, A. L.; Gamarra, D.; Munuera, G.; Martínez-Arias, A. CO-TPR-DRIFTS-MS in situ study of CuO/$Ce_{1-x}Tb_xO_{2-y}$ (x = 0, 0.2 and 0.5) catalysts: Support effects on redox properties and CO oxidation catalysis. *J. Catal.* **2009**, *268*, 367−375.
(58) Manzoli, M.; Monte, R. D.; Boccuzzi, F.; Coluccia, S.; Kašpar, J. CO oxidation over $CuO_x$-$CeO_2$-$ZrO_2$ catalysts: Transient behavior and role of copper clusters in contact with ceria. *Appl. Catal. B: Environ.* **2005**, *61*, 192−205.
(59) Wang, W.; Yu, W.; Du, P.; Xu, H.; Jin, Z.; Si, R.; Ma, C.; Shi, S.; Jia, C.; Yan, C. Crystal plane effect of ceria on supported copper oxide cluster catalyst for CO oxidation: Importance of metal−support interaction. *ACS Catal.* **2017**, *7*, 1313−1329.
(60) Wan, H.; Wang, Z.; Zhu, J.; Li, X.; Liu, B.; Gao, F.; Dong, L.; Chen, Y. Influence of CO pretreatment on the activities of CuO/$\gamma$-$Al_2O_3$ catalysts in CO+$O_2$ reaction. *Appl. Catal. B: Environ.* **2008**, *79*, 254−261.
(61) Polychronopoulou, K.; AlKhoori, A. A.; Efstathiou, A. M.; Jaoude, M. A.; Damaskinos, C. M.; Baker, M. A.; Almutawa, A.; Anjum, D. H.; Vasiliades, M. A.; Belabbes, A.; Vega, L. F.; Zedan, A. F.; Hinder, S. J. Design aspects of doped $CeO_2$ for low-temperature catalytic CO oxidation: Transient kinetic and DFT approach. *ACS Appl. Mater. Interfaces* **2021**, *13*, 22391−22415.
(62) Nyathi, T. M.; Fadlalla, M. I.; Claeys, M. In situ and Operando Characterization in the Preferential Oxidation of Carbon Monoxide over Base Metal Oxide Catalysts: A Review. *Chem. Catal. Chem.* **2024**, *16*, No. e202400285.

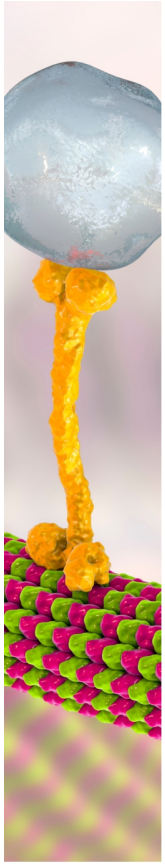
CAS BIOFINDER DISCOVERY PLATFORM™
BRIDGE BIOLOGY AND CHEMISTRY FOR FASTER ANSWERS
Analyze target relationships, compound effects, and disease pathways
Explore the platform
CAS
A division of the American Chemical Society



https://doi.org/10.1021/acscatal.5c06757
*ACS Catal.* 2026, 16, 5499−5519